Verification of 2D x 2D and two-species Vlasov-Poisson solvers

Yann A Barsamian, Joackim Bernier, Sever Adrian Hirstoaga, Michel
Mehrenberger

Verification of $2D \times 2D$ and two-species Vlasov-Poisson solvers

Y. Barsamian, J. Bernier, S. A. Hirstoaga, M. Mehrenberger

December 20, 2017

Abstract

In [18], $1D \times 1D$ two-species Vlasov-Poisson simulations are performed by the semi-Lagrangian method. Thanks to a classical first order dispersion analysis, we are able to check the validity of their simulations; the extension to second order is performed and shown to be relevant for explaining further details. In order to validate multi-dimensional effects, we propose a $2D \times 2D$ single species test problem that has true $2D$ effects coming from the sole second order dispersion analysis.

Finally, we perform, in the same code, full $2D \times 2D$ non linear two-species simulations with mass ratio $\sqrt{0.01}$, and consider the mixing of semi-Lagrangian and Particle-in-Cell methods.

1 Introduction

We consider the two-species Vlasov-Poisson system in $2D \times 2D$. We look for ion and electron distribution functions $f_s = f_s(t, x, v)$, with $s \in \{e, i\}$ and electric field $E = E(t, x)$, satisfying

$$\begin{cases} \partial_t f_i + v \cdot \nabla_x f_i + \frac{q}{m_i} E \cdot \nabla_v f_i = 0, \\ \partial_t f_e + v \cdot \nabla_x f_e - \frac{q}{m_e} E \cdot \nabla_v f_e = 0, \\ -\varepsilon_0 \Delta_x \Phi = q \int_{\mathbb{R}^2} f_i - f_e \, dv, \\ -\nabla_x \Phi = E. \end{cases} \tag{1}$$

and subject to initial distributions $f_i(t = 0, x, v)$ and $f_e(t = 0, x, v)$. Here q is the charge, m_s is the mass of the species s and ε_0 is the dielectric constant, $t \in \mathbb{R}^+$ is the time, $x = (x_1, x_2) \in \Omega_x = \mathbb{R}^2/(L_1\mathbb{Z} \times L_2\mathbb{Z})$ the position and $v \in \mathbb{R}^2$ the velocity. $\Phi = \Phi(t, x)$ is the electric potential. The original aim of the PICSL Cemracs project is to develop a code that works both for Particle-in-Cell (PIC) and semi-Lagrangian (SL) method and that is able to solve equation (1). We focus here on some of the difficulties of kinetic simulations that are the multi-dimensionality (here $2D \times 2D$ instead of $1D \times 1D$), multi-species (ions and electrons) and multi-methods (both PIC and SL) aspects. Extensions to higher dimensions, Vlasov-Maxwell (see [26] for such a recent work, that discusses also the pros/cons between PIC and semi-Lagrangian methods) and gyrokinetics (that includes the issue of using more complex geometries) is out of the scope of this paper and will be the subject of further research.

In the literature, works on single species $1D \times 1D$ Vlasov-Poisson solvers is abundant. We refer here to [23, 21, 14, 12, 13, 10, 3, 2, 1, 15, 19, 24] for works on $2D \times 2D$ Vlasov-Poisson simulations and to [18, 17] on multi-species simulations. This list is far from being exhaustive; there is a huge number of papers in plasma physics on the subject. Validation with respect to the dispersion relation is often performed for $1D \times 1D$ simulations (see for example [22], where cross code comparison is also performed). The dispersion relation analysis, even if less used, permits also to study multi-dimensional and multi-species simulations.

Using such an analysis, our first aim is to justify the two-species simulations of [18], following [25], and consisting in the linearization of the equations around the Maxwellian equilibrium. Note that the dispersion analysis dates back to Landau [16]. With respect to the usual single species case, two main modes play here a role and their relative weights have an importance, in order to catch the right behavior. A finer study permits to exhibit relevant nonlinear effects, thanks to a second order expansion.

We then had in mind to extend the results to the multi-dimensional case. We focus there first on the single species case and are able to show a *true* multi-dimensional effect solely visible from a second order expansion. Note that in the literature, usual $2D \times 2D$ test cases reduce to $1D \times 1D$ (see previous references based on Landau and two-stream instabilities test cases; note that in [19], an effort has been put to get a two dimensional character). We then could study the two-species case, in the $2D \times 2D$ setting, but such analysis is basically the superposition of the two previous analysis and we prefer here to focus on performing nonlinear simulations, where the analysis coming from the dispersion relation is anyway no more valid.

If a subsequent part of the work relies on the verification of the codes through the dispersion relation, another part of the work is based on the comparison and the mixing of semi-Lagrangian and PIC methods. As the two methodologies are quite different, getting the same answers for both codes is a further validation. On the other hand, defining a common code that works for both of them is a step to allow for a wider application range, as each method has his own benefits and drawbacks. We could for example consider in the future, the PIC method when a species is well localized (which permits to prevent from the discretization of the whole phase space) and the semi-Lagrangian method for other species. Note that the coupling of the two methods seems not to have been considered; at least, such approach is rare, as generally one method is privileged for a given simulation. The difficulties rely here on the definition of a common framework and on the need of expertise in both methods. In the numerical results, we will see that the present approach does not generate extra problems due to the coupling of the methods, which is encouraging for further developments.

In the sequel, we will first work on getting analytical results for our system, through the study of the dispersion relation. The analysis will be upgraded to second order expansion as done in [11], for example. This will enable us to propose the *true* $2D \times 2D$ one species test case and also to study the two-species ($1D \times 1D$) test case proposed by Badsi-Herda [18]. We will then present the numerical method and implementation details that permit to deal with both methods, before giving the numerical results, which are in accordance with the analytical results. We then present full non linear two-species results in $2D \times 2D$ (an extension to two-species of a test case presented in [19]). Finally we give some details about the efficiency of the code in the context of parallel programming on supercomputers.

2 Description of the equations and test cases

In this section, we describe the test cases and motivate our work.

2.1 A $1D \times 1D$ two-species test case

The first test case has been studied by [18]. We look for f_i, f_e satisfying

$$\begin{cases} \partial_t f_i + v \, \partial_x f_i + E \, \partial_v f_i = 0, \\ \partial_t f_e + \frac{1}{\varepsilon} v \, \partial_x f_e - \frac{1}{\varepsilon} E \, \partial_v f_e = 0, \\ \partial_x E = \int_{\mathbb{R}} f_i - f_e dv, \text{ with } \varepsilon = \sqrt{\frac{m_e}{m_i}}, \text{ the root of the mass ratio between ions and electrons.} \end{cases} \tag{2}$$

The initial functions are given by

$$\begin{cases} f_e(0, x, v) = \frac{1}{\sqrt{2\pi}} e^{-\frac{v^2}{2}}, \\ f_i(0, x, v) = \frac{v^2}{\sqrt{2\pi}\sigma^3} e^{-\frac{v^2}{2\sigma^2}} (1 + A \cos(kx)), \end{cases} \tag{3}$$

with $k = \frac{2\pi}{L}$, and A the amplitude of the perturbation. The phase-space domain is $[0, L] \times [-v_{\max}, v_{\max}]$. We will take here $\sigma = \frac{1}{2}$ and $L = 21$, as in [18].

This is a first example of two-species simulation. Our goal is to reproduce these results [18] from the literature with our commonly used methods (as in [20] for example) and also to provide a dispersion analysis, which permits to further validate the code. Note that this test is $1D \times 1D$, but it will be simulated in the $2D \times 2D$ code; this enables to have a first check of the code.

2.2 A $2D \times 2D$ one-species test case

We focus then on $2D \times 2D$ phase space. We look for f satisfying

$$\begin{cases} \partial_t f + v \cdot \nabla_x f - E \cdot \nabla_v f = 0, \\ -\Delta_x \Phi = 1 - \int_{\mathbb{R}^2} f dv, \\ -\nabla_x \Phi = E, \end{cases} \tag{4}$$

with initial function

$$f(0, x, v) = \left(1 + A \left(\cos(\frac{x_2}{2}) + \cos(\frac{x_1 + x_2}{2})\right)\right) \frac{v_1^2}{2\pi} e^{-\frac{|v|^2}{2}}. \tag{5}$$

We take $L_1 = L_2 = 4\pi$, the phase-space domain is $[0, 4\pi]^2 \times [-v_{\max}, v_{\max}]^2$ and $v_{\max} = 10$.

This test permits to capture the interaction of different modes and reveals $2D$ space features, which would not be visible by $1D \times 1D$ codes. The authors are not aware of such a test case in the literature; it seems not to be standard.

2.3 A $2D \times 2D$ two-species test case

We look for f_i, f_e satisfying

$$\begin{cases} \partial_t f_i + v \cdot \nabla_x f_i + E \cdot \nabla_v f_i = 0, \\ \partial_t f_e + \frac{1}{\varepsilon} v \cdot \nabla_x f_e - \frac{1}{\varepsilon} E \nabla_v f_e = 0, \\ \nabla_x \cdot E = \int_{\mathbb{R}^2} f_i - f_e dv, \text{ with } \varepsilon = \sqrt{\frac{m_e}{m_i}}, \text{ the root of the mass ratio between ions and electrons.} \end{cases} \tag{6}$$

The initial functions are given by

$$\begin{cases} f_e(0, x, v) = \frac{1}{2\pi} e^{-\frac{v^2}{2}}, \\ f_i(0, x, v) = \frac{1}{4\pi\sigma_1\sigma_2} \left(1 - A_1 \sin(k_1 x_1) - A_2 \sin(k_2 x_2)\right) \left(e^{-\frac{(v_1 - v_d)^2}{2\sigma_1^2}} + e^{-\frac{(v_1 + v_d)^2}{2\sigma_1^2}}\right) e^{-\frac{v_2^2}{2\sigma_2^2}}, \end{cases} \tag{7}$$

with $k_1 = \frac{2\pi}{L_1}$, $k_2 = \frac{2\pi}{L_2}$, the perturbation amplitudes A_1, A_2, the velocity drift v_d and the thermal velocities σ_1, σ_2. The domain is $[0, L_1] \times [0, L_2] \times [-v_{\max}, v_{\max}]^2$.

Our aim is to develop $2D \times 2D$ two-species simulations; so, here is such an example. It is a generalization of the first test to the $2D \times 2D$ framework; we use a $2D \times 2D$ initial function for the ions that was developed in [19]. We will take here $v_d = 2.4$, $A_1 = 0.005$, $A_2 = 0.25$, $\sigma_1 = 0.5$, $\sigma_2 = 1$, $k_1 = k_2 = 0.2$ together with $v_{\max} = 10$.

3 Dispersion analysis

In this section, we perform the dispersion analysis for the first and second test cases (Subsection 2.1 and 2.2). The dispersion analysis consists in studying a perturbation of an equilibrium solution, which leads formally to a solution of the linearized problem. For the first test case, we obtain in particular the behavior in the mass ratio limit $\varepsilon \to 0$. A finer analysis using second order expansion permits to explain an instability that cannot be captured through first order expansion. Such an expansion will also be a key in the development of the second test case (Subsection 2.2).

3.1 First order expansion

We first recall the first order expansion with respect to A, in the simplest case and then look how to adapt it to multi-dimensional and multi-species cases. The procedure is quite standard. We give here the general form and explicit the computations for Maxwellian type initial functions.

3.1.1 The one dimensional case with one species.

We first recall the $1D \times 1D$ dispersion analysis (see [25] for details). Taking an initial condition of the form

$$f(t = 0, x, v) = f^0(v) + A f^1(t = 0, x, v), \quad \int f_0(v) dv = 1$$

and look for a solution

$$f(t, x, v) = f^0(v) + A f^1(t, x, v), E(t, x) = A E^1(t, x)$$

of the Vlasov-Poisson equation

$$\begin{cases} \partial_t f + v \partial_x f - E \partial_v f = 0, \\ \partial_x E = 1 - \int f dv, \end{cases}$$

neglecting $O(A^2)$ terms. We then get an equation for f_1 which reads

$$\begin{cases} \partial_t f_1 + v \partial_x f_1 - E^1 \partial_v f_0 = 0, \\ \partial_x E^1 = - \int f^1 dv, \end{cases} \tag{8}$$

Considering $f^1(t=0,x,v) = \widehat{f}(t=0,v)e^{ikx}$ with $k \in \frac{2\pi}{L}\mathbb{Z}^*$, we get a solution of (8) which is

$$\begin{cases} \partial_t \widehat{f} + ivk\widehat{f} - \widehat{E}(t)\partial_v f^0 = 0, \\ ik\widehat{E} = -\int_{\mathbb{R}} \widehat{f}dv, \end{cases} \tag{9}$$

with $E^1 = \widehat{E}(t)e^{ikx}$. In order to express E, we introduce D_k and N_k defined by

$$\begin{cases} D_k(\omega) = 1 - \frac{1}{k^2}\int_{\mathbb{R}} \frac{\partial_v f^0}{v-\frac{\omega}{k}}dv, \\ N_k(\omega) = \frac{1}{k^2}\int_{\mathbb{R}} \frac{\widehat{f}(0,v)}{v-\frac{\omega}{k}}dv, \end{cases} \tag{10}$$

and get thanks to a Laplace transform and the theorem of residuals

$$\widehat{E}(t) = \sum_{\omega \in D_k^{-1}(\{0\})} Res_\omega e^{-i\omega t}, \text{ where } Res_\omega = \frac{N_k(\omega)}{\partial_\omega D_k(\omega)},$$

which leads to an expression of E whose L^2 norm will be computed as a diagnostic in the numerical results.

3.1.2 The one dimensional case with m species.

Considering $f_j : \mathbb{R}_+ \times \mathbb{R}/L\mathbb{Z} \times \mathbb{R} \to \mathbb{R}$, $j = 1, \dots, m$, satisfying

$$\begin{cases} \partial_t f_j + a_j v \partial_x f_j + b_j E \partial_v f_j = 0, \ j = 1, \dots, m \\ \partial_x E = \sum_{j=1}^m \int_{\mathbb{R}} z_j f_j dv, \end{cases}$$

with general numbers a_j, b_j, z_j. We get similarly the solution of the linearized problem which writes

$$f_j = f_j^0(v) + A f_j^1, \ f_j^1 = \widehat{f}_j(t,v)e^{ikx}, \ j = 1, \dots, m, \text{ and } E^1 = Ae^{ikx}\widehat{E},$$

where f_j^1 and E^1 satisfy

$$\begin{cases} \partial_t f_j^1 + a_j v \partial_x f_j^1 + b_j E^1 \partial_v f_j^0 = 0, \ j = 1, \dots, m \\ \partial_x E^1 = \sum_{j=1}^m \int_{\mathbb{R}} z_j f_j^1 dv, \end{cases}$$

and are given by the expressions

$$\widehat{E}(t) = \sum_{\omega \in D_k^{-1}(\{0\})} Res_\omega e^{-i\omega t},$$

with

$$Res_\omega = \frac{N_k(\omega)}{\partial_\omega D_k(\omega)},$$

and

$$\begin{cases} D_k(\omega) = 1 - \frac{1}{k^2}\sum_{j=1}^m b_j \frac{z_j}{a_j}\int_{\mathbb{R}} \frac{\partial_v f_j^0}{v-\frac{\omega}{a_j k}}dv, \\ N_k(\omega) = -\frac{1}{k^2}\sum_{j=1}^m \frac{z_j}{a_j}\int_{\mathbb{R}} \frac{\widehat{f}_j(0,v)}{v-\frac{\omega}{a_j k}}dv. \end{cases} \tag{11}$$

We then can further explicit these computations, for Maxwellian type functions, thanks to the plasma dispersion function of Fried and Conte (see [25])

$$Z(\xi) = \frac{1}{\sqrt{\pi}}\int_{\mathbb{R}} \frac{e^{-v^2}}{v-\xi}dv = \sqrt{\pi}e^{-\xi^2}(i - \text{erfi}(\xi)), \ \text{erfi}(\xi) = \frac{2}{\sqrt{\pi}}\int_0^\xi e^{z^2}dz.$$

In (11), we typically can have terms like

$$\int_{\mathbb{R}} \frac{(v-v_d)^\ell \exp\left(-\frac{(v-v_d)^2}{2\sigma^2}\right)}{v-\alpha}dv = \int_{\mathbb{R}} \frac{v^\ell \exp\left(-\frac{v^2}{2\sigma^2}\right)}{v-(\alpha-v_d)}dv = (\sqrt{2}\sigma)^\ell \int_{\mathbb{R}} \frac{v^\ell \exp\left(-v^2\right)}{v-\frac{\alpha-v_d}{\sqrt{2}\sigma}}dv = \sqrt{\pi}(\sqrt{2}\sigma)^\ell Z_\ell\left(\frac{\alpha-v_d}{\sqrt{2}\sigma}\right),$$

and

$$\int_{\mathbb{R}} \frac{\partial_v\left((v-v_d)^\ell \exp\left(-\frac{(v-v_d)^2}{2\sigma^2}\right)\right)}{v-\alpha}dv = \sqrt{\pi}(\sqrt{2}\sigma)^{\ell-1}\left(-2Z_{\ell+1}\left(\frac{\alpha-v_d}{\sqrt{2}\sigma}\right) + \ell Z_{\ell-1}\left(\frac{\alpha-v_d}{\sqrt{2}\sigma}\right)\right),$$

4

defining

$$Z_\ell(\xi) := \frac{1}{\sqrt{\pi}} \int_{\mathbb{R}} \frac{v^\ell \exp\left(-v^2\right)}{v - \xi} dv.$$

We have from Appendix B of [6]

$$Z_\ell(\xi) = \frac{(-1)^\ell}{2^\ell} \sum_{j=0}^{\lfloor \ell/2 \rfloor} d_j(\ell) Z^{(\ell-2j)}(\xi), \ d_j(\ell) = \frac{\ell(\ell-1)\ldots(\ell-2j+1)}{j!},$$

with the derivatives

$$Z^{(0)}(\xi) = Z(\xi), \ Z^{(1)}(\xi) = -2(1 + \xi Z(\xi)), \ Z^{(n)}(\xi) = -2((n-1)Z^{(n-2)}(\xi) + \xi Z^{(n-1)}(\xi)), \ n \geq 2.$$

The first terms are $Z_0 = Z$ and

$$
\begin{aligned}
Z_1 &= \xi Z + 1, & Z_2 &= \xi^2 Z + \xi, \\
Z_3 &= \xi^3 Z + \xi^2 + \tfrac{1}{2}, & Z_4 &= \xi^4 Z + \xi^3 + \tfrac{1}{2}\xi, \\
Z_5 &= \xi^5 Z + \xi^4 + \tfrac{1}{2}\xi^2 + \tfrac{3}{4}, & Z_6 &= \xi^6 Z + \xi^5 + \tfrac{1}{2}\xi^3 + \tfrac{3}{4}\xi, \\
Z_7 &= \xi^7 Z + \xi^6 + \tfrac{1}{2}\xi^4 + \tfrac{3}{4}\xi^2 + \tfrac{15}{8}, & Z_8 &= \xi^8 Z + \xi^7 + \tfrac{1}{2}\xi^5 + \tfrac{3}{4}\xi^3 + \tfrac{15}{8}\xi.
\end{aligned}
$$

In fact, we can check that we have the following formula:

$$Z_{2p+1} = \xi^{2p}(\xi Z + 1) + \sum_{\ell=1}^{p} \xi^{2p-2\ell} \prod_{j=1}^{\ell} (j - \frac{1}{2}), \ Z_{2p+2} = \xi Z_{2p+1}.$$

In particular, for the first two-species test case (described in Subsection 2.1), we define $\xi_i = \frac{\omega}{\sqrt{2}k\sigma}$ and $\xi_e = \frac{\omega\varepsilon}{\sqrt{2}k}$. We get

$$D_k(\omega) = 1 - \frac{\sqrt{\pi}}{k^2}\left(\frac{2\sqrt{2}\sigma}{\sqrt{2\pi}\sigma^3}(-Z_3(\xi_i) + Z_1(\xi_i)) - \frac{\sqrt{2}}{\sqrt{2\pi}}Z_1(\xi_e)\right), \ N_k(\omega) = -\frac{\sqrt{\pi}}{\sqrt{2\pi}k^2}\frac{(\sqrt{2}\sigma)^2}{\sigma^3}Z_2(\xi_i).$$

This leads to

$$D_k(\omega) = 1 - \frac{1}{k^2}\left(\frac{2}{\sigma^2}\left(-\xi_i^3 Z(\xi_i) + \xi_i Z(\xi_i) - \xi_i^2 - \frac{1}{2} + 1\right) - \xi_e Z(\xi_e) - 1\right), N_k(\omega) = -\frac{1}{\sqrt{2}k^2}\frac{2}{\sigma}Z_2(\xi_i).$$

Finally, we have

$$
\begin{cases}
D_k(\omega) = 1 - \frac{1}{k^2}\left(\frac{1}{\sigma^2} - 1 + \frac{2}{\sigma^2}\left(\xi_i(1-\xi_i^2)Z(\xi_i) - \xi_i^2\right) - \xi_e Z(\xi_e)\right), \\
N_k(\omega) = -\frac{1}{\sqrt{2}k^2}\frac{2}{\sigma}(\xi_i^2 Z(\xi_i) + \xi_i).
\end{cases}
\tag{12}
$$

In the sequel, we will write $D_k(\omega, \varepsilon)$, instead of $D_k(\omega)$ to specify the dependence of this quantity to ε, through $\xi_e = \frac{\omega\varepsilon}{\sqrt{2}k}$.

3.1.3 Asymptotic behavior for the two-species case

In the previous example, we remark that, in practice, it may be difficult to determinate the zeros of $D_k(\cdot, \varepsilon)$ when ε is small. As a consequence, we focus here on the asymptotic behavior of the zeros of $D_k(\cdot, \varepsilon)$, when ε goes to 0.

In this study, we consider $D_k(\cdot, \varepsilon)$ as a continuous family of entire functions. By the classical holomorphic function theory, there exists a family of continuous functions (ω_n) of the variable ε, indexed by a set of natural integers $\mathscr{S}$, such that for all ε, $\{\omega_n(\varepsilon) \mid n \in \mathscr{S}\}$ is the set of the zeros of $D_k(\cdot, \varepsilon)$. We can determine the asymptotic behavior of these functions as $\varepsilon \to 0$.

Defining

$$\Delta_i(\xi) := 1 - \frac{1}{k^2}\left(\frac{1}{\sigma^2} - 1 + \frac{2}{\sigma^2}\xi(1-\xi^2)Z(\xi) - \frac{2}{\sigma^2}\xi^2\right), \ \Delta_e(\xi) := 1 + \frac{1}{k^2}\left(1 + \xi Z(\xi)\right)$$

we have

$$\Delta_i(\xi) = \lim_{\xi_e \to 0, \ \xi_i = \xi} D_k, \ \Delta_e(\xi) = \lim_{\xi_i \to \infty, \ \xi_e = \xi} D_k,$$

considering here D_k as a function of ξ_e and ξ_i. The latter limit is obtained thanks to the limits

$$\xi Z(\xi) \xrightarrow[\xi \to \infty]{} -1, \ \xi^3 Z(\xi) + \xi^2 \xrightarrow[\xi \to \infty]{} -\frac{1}{2},$$

5

coming from the asymptotic expansion

$$Z(\xi) = \sqrt{\pi}e^{-\xi^2}\left(i - \frac{\xi}{\sqrt{-\xi^2}}\right) - \frac{1}{\xi} - \frac{1}{2\xi^3} + O\left(\frac{1}{\xi^5}\right). \tag{13}$$

We have more precisely the following result, which gives the asymptotic location of the zeros of D_k when $\varepsilon \to 0$.

Proposition 3.1. *We define* $\xi_i(\omega) = \frac{\omega}{\sqrt{2k\sigma}}$, $\xi_e(\omega,\varepsilon) = \frac{\omega\varepsilon}{\sqrt{2k}}$. *For all* $n \in \mathscr{S}$,

- *either* $\xi_i(\omega_n(\varepsilon))$ *converges, when* ε *tends to 0, to a zero of* Δ_i,

- *either* $\xi_i(\omega_n(\varepsilon))$ *goes to infinity and* $\xi_e(\omega_n(\varepsilon),\varepsilon)$ *converges, as* ε *tends to 0, to a zero of* Δ_e,

- *either* $\xi_i(\omega_n(\varepsilon))$ *goes to infinity and the argument of* $\omega_n(\varepsilon)$ *converges, as* ε *tends to 0, to* $-\frac{3\pi}{4}$ *or to* $-\frac{\pi}{4}$.

Proof. See Appendix 8.1. □

3.1.4 The multi-dimensional case.

When we consider the d-dimensional case ($d \geq 1$) with one species case[1], we take an initial condition of the form

$$f(t=0,x,v) = f^0(v) + A\widehat{f}(t=0,v)e^{ik\cdot x},$$

and look for a solution

$$f(t,x,v) = f^0(v) + Af^1(t,x,v), \ f^1(t,x,v) = \widehat{f}(t,v)e^{ik\cdot x}, \ k \in \frac{2\pi}{L_1}\mathbb{Z} \times \cdots \times \frac{2\pi}{L_d}\mathbb{Z},$$

where f^1 solves

$$\begin{cases} \partial_t f^1 + v \cdot \nabla_x f^1 - E^1 \cdot \nabla_v f^0 = 0 \\ \nabla \cdot E^1 = -\int f^1 dv. \end{cases}$$

We introduce the component of the velocity along the mode k and its orthogonal:

$$v = v_\| e_k + \sum_{j=1}^{d-1} v_{\perp,j} e_k^{\perp,j} \text{ where } e_k := \frac{k}{|k|},$$

and $\{e_k, e_k^{\perp,j}, \ j = 1, \ldots, d-1\}$ is an orthogonal basis of $\mathbb{R}^d$.

Note that this analysis is already present in the original work of Landau [16]. There he considered, e_k is along the x-direction. We detail here the computations, without assuming this simplification, which permits later (see Subsection 3.2) to consider several modes, and their interactions. The analog to (9) is

$$\begin{cases} \partial_t \widehat{f} + i(v \cdot k)\widehat{f} - \widehat{E} \cdot \nabla_v f^0 = 0, \\ \widehat{E} = \frac{ik}{|k|^2}\int \widehat{f}dv, \end{cases}$$

with $E^1(t,x) = \widehat{E}(t)e^{ik\cdot x}$. As E is along k, we obtain

$$\begin{cases} \partial_t \widehat{f} + i(v_\||k|)\widehat{f} - (\widehat{E} \cdot e_k)\partial_{v_\|}f^0 = 0, \\ \widehat{E} = \frac{ik}{|k|^2}\int \widehat{f}dv = (\widehat{E} \cdot e_k)e_k. \end{cases} \tag{14}$$

Note that there is no evolution in $v_\perp$. We now integrate the equation in $v_\perp$. Introducing the notation $< . >_\perp$ defined by

$$< g >_\perp (v_\|) = \int_\mathbb{R} g\left(v_\| e_k + \sum_{j=1}^{d-1} v_{\perp,j} e_k^{\perp,j}\right)dv_{\perp,1}\ldots dv_{\perp,d-1},$$

we get

$$\begin{cases} \partial_t < \widehat{f} >_\perp +i(v_\||k|) < \widehat{f} >_\perp -(\widehat{E} \cdot e_k)\partial_{v_\|} < f^0 >_\perp = 0, \\ \widehat{E} = \frac{ik}{|k|^2}\int < \widehat{f} >_\perp dv_\| = (\widehat{E} \cdot e_k)e_k. \end{cases}$$

---

[1]a similar expression is straightforward for the multi-species case

We finally can reuse the one-dimensional analysis and the first order dispersion relation rewrites

$$\widehat{E}(t) = \sum_{\omega \in D_k^{-1}(\{0\})} Res_\omega e^{-i\omega t} e_k,$$

with

$$Res_\omega = \frac{N_k(\omega)}{\partial_\omega D_k(\omega)},$$

where

$$\begin{cases} D_k = 1 - \frac{1}{|k|^2} \int_{\mathbb{R}} \frac{\partial_{v_\parallel} <f^0>_\perp(v_\parallel)}{v_\parallel - \frac{\omega}{|k|}} dv_\parallel, \\ N_k = \frac{1}{|k|^2} \int_{\mathbb{R}} \frac{<\widehat{f}>_\perp(0,v_\parallel)}{v_\parallel - \frac{\omega}{|k|}} dv_\parallel. \end{cases} \tag{15}$$

3.2 Second order expansion

3.2.1 Introduction

We focus here on second order expansion with respect to A; such expansion has been developed in [11] for example for the Landau damping. Through the previous first order analysis, we can get the superposition of $1D$ modes. Indeed we can consider an initial function of the form

$$f(t = 0, x, v) = f^0(v) + A \sum_{k \in \mathcal{K}} \widehat{f}_k(0, v) e^{ik \cdot x},$$

for a given set of modes $\mathcal{K}$ and get a linearized solution of the form

$$E(t, x) = \sum_{k \in \mathcal{K}} \sum_{\omega \in D_k^{-1}(\{0\})} Res_\omega e^{-i\omega t} e^{ik \cdot x} e_k. \tag{16}$$

Note that in this expression, we do not see the multi-dimensional (non-linear) interaction of these modes. Thanks to a second order expansion, we are able to study the interaction of different modes in space and design test cases more relevant to the dimension 2 (second test case, Subsection 2.2). As a by product, it will also be useful to better qualitatively describe the first $1D$ two-species test case of Subsection 2.1.

3.2.2 Results

We look for solutions of the one species Vlasov-Poisson system set for $x \in [0, L_1] \times \ldots \times [0, L_d]$ and $v \in \mathbb{R}^d$ in the form

$$f(t, x, v) = f_0(v) + A f_1(t, x, v) + A^2 f_2(t, x, v) \text{ and } E(t, x) = A E_1(t, x) + A^2 E_2(t, x).$$

We assume that $f_2(0, x, v) = 0$, and take initially

$$f_1(t = 0, x, v) = \sum_{k \in \mathcal{K}} \widehat{f}_k(0, v) e^{ik \cdot x}, \ \mathcal{K} \subset \frac{2\pi}{L_1} \mathbb{Z} \times \cdots \times \frac{2\pi}{L_d} \mathbb{Z}.$$

Let $g = S(t)u$ be the solution of the homogeneous system

$$\begin{cases} \partial_t g + v \cdot \nabla_x g - E(g) \cdot \nabla_v f_0 = 0, \\ \nabla_x \cdot E(g) = - \int_{\mathbb{R}^d} g dv, \\ g(t = 0, \cdot, \cdot) = u. \end{cases}$$

Let $u = c_k(v) e^{ik \cdot x}$, with $k \in \frac{2\pi}{L_1} \mathbb{Z} \times \cdots \times \frac{2\pi}{L_d} \mathbb{Z}$ such that $\int_{\mathbb{R}^d} c_k(v) dv = 0$, when $k = 0$. We have

$$E(S(t)u)(x) = \begin{cases} \sum_{\omega \in D_k^{-1}(\{0\})} \frac{N_k(\omega, c_k)}{\partial_\omega D_k(\omega)} e^{-i\omega t} e^{ik \cdot x} e_k, \text{ if } k \neq 0 \\ 0, \text{ if } k = 0, \end{cases} \tag{17}$$

with the definition

$$N_k(\omega, h) = \frac{1}{|k|^2} \int \frac{h(v)}{v \cdot e_k - \frac{\omega}{|k|}} dv, \text{ for } h \text{ a function of } v,$$

valid for $k \neq 0$.

Proceeding as usual by linearization (see the previous analysis) we find the classical equation for f_1 and E_1. Then, we obtain f_2 and E_2 as solutions of

$$
\begin{cases}
\partial_t f_2 + v \cdot \nabla_x f_2 - E_2 \cdot \nabla_v f_0 - E_1 \cdot \nabla_v f_1 = 0, \\
\nabla_x \cdot E_2 = - \int_{\mathbb{R}^d} f_2 dv.
\end{cases}
\tag{18}
$$

First, we deduce from (18) that we can look for the modes $k \neq 0$ for E_2. Indeed, since $\int \int f_2 dv dx = 0$, which is a consequence of the hypothesis $f_2(0, x, v) = 0$, the Poisson equation in (18) admits, modulo a constant, a unique solution for the electric potential, which leads to $\int E_2 dx = 0$.

Then, thanks to the dispersion analysis we can compute the source term $E_1 \cdot \nabla_v f_1$ above. Therefore, by the Duhamel formula we can write

$$
f_2(t, \cdot, \cdot) = S(t) f_2(0, \cdot, \cdot) + \int_0^t S(t - s)(E_1(s, \cdot) \cdot \nabla_v f_1(s, \cdot, \cdot)) ds.
$$

As $f_2(0, \cdot, \cdot) = 0$, we get

$$
f_2(t, \cdot, \cdot) = \int_0^t S(t - s)(E_1(s, \cdot) \cdot \nabla_v f_1(s, \cdot, \cdot)) ds.
$$

Inserting E_1 and f_1 which are of the form

$$
E_1(t, x) = \sum_{k \in \mathcal{K}} \widehat{E}_k(t) e^{ik \cdot x} e_k, \quad f_1(t, x, v) = \sum_{k \in \mathcal{K}} \widehat{f}_k(t, v) e^{ik \cdot x},
$$

we get

$$
f_2(t, x, v) = \sum_{k' \in \mathcal{K}} \sum_{k'' \in \mathcal{K}} \int_0^t S(t - s)(\widehat{E}_{k'}(s) e_{k'} \cdot \nabla_v \widehat{f}_{k''}(s, v) e^{i(k' + k'') \cdot x}) ds.
$$

Now, thanks to the linearity of $f \mapsto E[f]$, we have

$$
E_2(t, \cdot) = E[f_2(t, \cdot, \cdot)] = \sum_{k' \in \mathcal{K}} \sum_{k'' \in \mathcal{K}} \int_0^t E[(x, v) \mapsto S(t - s)(\widehat{E}_{k'}(s) e_{k'} \cdot \nabla_v \widehat{f}_{k''}(s, v) e^{i(k' + k'') \cdot x})] dt
$$

Using (17), we get

$$
E_2(t, x) = \sum_{(k', k'') \in \mathcal{K}, \ k' \neq -k''} \sum_{\omega \in D_{k' + k''}^{-1}(\{0\})} \left(\int_0^t \widehat{E}_{k'}(s) N_{k' + k''}(\omega, e_{k'} \cdot \nabla_v \widehat{f}_{k''}(s, \cdot)) e^{-i\omega(t-s)} dt \right) \frac{e^{i(k' + k'') \cdot x}}{\partial_\omega D_{k' + k''}(\omega)} e_{k' + k''},
$$

where $k' \neq -k''$ is due to the condition of $k \neq 0$ above.
We look for the dependence in time of this expression.
We write

$$
E_2(t, x) = \sum_{(k', k'') \in \mathcal{K}, \ k' \neq -k''} \hat{\mu}_{k' + k''} e^{i(k' + k'') \cdot x} e_{k' + k''}.
$$

The expansion of $\hat{\mu}_{k' + k''}$ makes appear terms like $e^{-i\omega t}$ and $e^{-i(\omega' + \omega'')t}$, where $\omega \in D_k^{-1}(\{0\})$, $\omega' \in D_{k'}^{-1}(\{0\})$ and $\omega'' \in D_{k''}^{-1}(\{0\})$. A precise result related to this expansion is rather technical and will be detailed elsewhere.

4   Numerical method

In order to solve the Vlasov equation, we develop a code that is able to use both Particle-in-Cell (PIC) and semi-Lagrangian methods, in the framework of the Selalib[2] library. For the Poisson solver, we classically use the FFT; time and space (semi-Lagrangian or PIC) will be further detailed thereafter. The framework is such that we can use PIC for the two-species, semi-Lagrangian for the two-species, or PIC for one species and semi-Lagrangian for the other species.

---

[2]http://selalib.gforge.inria.fr/

4.1 Time discretization

We consider two types of time discretizations. The first one is based on a splitting by direction, as in [18] and the second one is a splitting by species.

4.1.1 Splitting first by direction

The algorithm can be sketched as in Figures 1 and 2 for the classical Strang splitting. This scheme can be generalized to higher order splitting; we will here use the classical 6th order splitting of Blanes and Moan [5], as in [7].

Parameters :
Δt, the time step.
$ncx \times ncy$, the size of the spatial grid.

Variables :
$f_{electrons}$, the distribution function (4d array for SL, array of particles for PIC).
$\rho[ncx][ncy]$, a 2d array containing the charge distribution.
$E[ncx][ncy]$, a 2d array containing the self-induced electric field.

Initialization :
1   Initialize $f_{electrons}$

Algorithm :
2   **Foreach** time iteration, **do**
3   Advection of $f_{electrons}$ in x over $\Delta t/2$ $\partial_t f_{electrons} + v \cdot \nabla_x f_{electrons} = 0$
4   Compute ρ from $f_{electrons}$ (integration in v for SL, deposit for PIC)
5   Compute E from ρ Poisson solver
6   Advection of $f_{electrons}$ in v over Δt $\partial_t f_{electrons} - E \cdot \nabla_v f_{electrons} = 0$
7   Advection of $f_{electrons}$ in x over $\Delta t/2$ $\partial_t f_{electrons} + v \cdot \nabla_x f_{electrons} = 0$
8   **End Foreach**

Figure 1: One species (electrons) pseudo-code.

Parameters :
Δt, the time step.
$ncx \times ncy$, the size of the spatial grid.
$\varepsilon = \sqrt{\dfrac{m_{electrons}}{m_{ions}}}$, the square root of the mass ratio.

Variables :
$f_{electrons}$ and f_{ions}, the distribution function for electrons and ions (4d arrays for SL, arrays of particles for PIC).
$\rho_{electrons}[ncx][ncy], \rho_{ions}[ncx][ncy]$ and $\rho[ncx][ncy]$, 2d arrays containing the charge distribution.
$E[ncx][ncy]$, a 2d array containing the self-induced electric field.

Initialization :
1   Initialize $f_{electrons}$ and f_{ions}

Algorithm :
2   **Foreach** time iteration, **do**
3   Advection of $f_{electrons}$ in x over $\Delta t/2$ $\partial_t f_{electrons} + (1/\varepsilon)v \cdot \nabla_x f_{electrons} = 0$
4   Advection of f_{ions} in x over $\Delta t/2$ $\partial_t f_{ions} + v \cdot \nabla_x f_{ions} = 0$
5   Compute $\rho_{electrons}$ from $f_{electrons}$ and ρ_{ions} from f_{ions} (integration in v for SL, deposit for PIC)
6   Compute E from $\rho = \rho_{ions} - \rho_{electrons}$ Poisson solver
7   Advection of $f_{electrons}$ in v over Δt $\partial_t f_{electrons} - (1/\varepsilon)E \cdot \nabla_v f_{electrons} = 0$
8   Advection of f_{ions} in v over Δt $\partial_t f_{ions} + E \cdot \nabla_v f_{ions} = 0$
9   Advection of $f_{electrons}$ in x over $\Delta t/2$ $\partial_t f_{electrons} + (1/\varepsilon)v \cdot \nabla_x f_{electrons} = 0$
10   Advection of f_{ions} in x over $\Delta t/2$ $\partial_t f_{ions} + v \cdot \nabla_x f_{ions} = 0$
11   **End Foreach**

Figure 2: Two-species pseudo-code, splitting by direction.

4.1.2 Splitting first by species

In order to have the possibility of dealing with the species differently, we developed another scheme based on a splitting by species. It is depicted in Figure 3.

Parameters :
Δt, the time step.
$ncx \times ncy$, the size of the spatial grid.
$\varepsilon = \sqrt{\dfrac{m_{electrons}}{m_{ions}}}$, the square root of the mass ratio.

Variables :
$f_{electrons}$ and f_{ions}, the distribution function for electrons and ions (4d arrays for SL, arrays of particles for PIC).
$\rho_{electrons}[ncx][ncy], \rho_{ions}[ncx][ncy]$ and $\rho[ncx][ncy]$, 2d arrays containing the charge distribution.
$E[ncx][ncy]$, a 2d array containing the self-induced electric field.

Initialization :
1   Initialize $f_{electrons}$ and f_{ions}

Algorithm :
2   **Foreach** time iteration, **do**
3   Solve Vlasov-Poisson (ions, $\Delta t/2$)
4   Solve Vlasov-Poisson (electrons, Δt)
5   Solve Vlasov-Poisson (ions, $\Delta t/2$)
6   **End Foreach**

Subroutine Solve Vlasov-Poisson (*species*, *time_step*) :
7   Advection of $f_{species}$ in x over *time_step*/2
8   Compute $\rho_{species}$ from f
9   Compute E from $\rho = \rho_{ions} - \rho_{electrons}$
10   Advection of $f_{species}$ in v over *time_step*
11   Advection of $f_{species}$ in x over *time_step*/2
12   Compute $\rho_{species}$ from $f_{species}$

Figure 3: Two-species pseudo-code, splitting by species.

Once more, this scheme can be generalized to higher order splitting. Nevertheless, we cannot use the splitting coefficients from the classical 6th order splitting, because they are not suitable for a splitting by species.

4.2 Semi-Lagrangian discretization

We use a classical backward semi-Lagrangian (BSL) method, consisting here in solving successive constant advection equations on a uniform $1D$ periodic mesh [9]. Centered Lagrange interpolation of degree 9 is used for the interpolation; see for example [20]. Concerning the splitting by species, we use Strang splitting on each species for the corresponding solving of the Vlasov-Poisson equation.

4.3 PIC discretization

A Particle-in-Cell (PIC) method consists in discretizing (sampling) the distribution function by a collection of N macro-particles that move in the phase space following the characteristics of the Vlasov equation. We use the classical PIC method, following the lines of [4], with linear or cubic splines for the deposition of the charge and for the interpolation of the electric field. The macro-particles are initialized randomly, which ensures a stochastic convergence in $\dfrac{1}{\sqrt{N}}$. All the results of this paper are shown with the random initialization.

Time schemes presented in Figures 1, 2 and 3 are still valid for the PIC method. These schemes are used when running simulations using PIC for one species and BSL for the other. However, to ensure efficiency when running simulations only with the PIC method, a leap-frog scheme is used (second order in time).

5 Numerical results

We now give the numerical results for the test cases described in Section 2.

5.1 First test case: $1D \times 1D$ two-species

This test case is described in Subsection 2.1. We take here $\varepsilon = 1$, as we first want here to validate the two-species feature; this permits to have a first example taken from the literature [18] that is here justified with the dispersion relation analysis and that can be cheaply reproduced in this one dimensional context. On Figure 4 (left, logarithmic scale; right, standard scale), we represent, for the perturbation $A = 0.0001$, the electric energy defined by $\sqrt{\frac{1}{2} \int_0^L |E|^2 dx}$ vs time t and also the absolute value of the first and second Fourier modes multiplied by $\sqrt{\frac{1}{2}}$, in order to be comparable to the electric energy. We represent also *theoretical* results, coming from the study of the dispersion analysis developed in Section 3. The theoretical first mode is here the expression

$$\mathcal{E}_1 = A \left| -0.1 \exp(0.089t) - 6.9 \cos(1.5t) \right|. \tag{19}$$

It comes from the first order dispersion relation whose more precise expression, using the two first relevant zeros, is

$$A \left| a_1 \exp(\gamma_1 t) + a_2 \exp(\gamma_2 t) \cos(\omega t) + a_3 \exp(\gamma_2 t) \sin(\omega t) \right|,$$

with

$$a_1 = -0.098626662403769140798, \ a_2 = -6.9231540740080643228, \ a_3 = -0.015835049471186903442,$$
$$\gamma_1 = 0.089001301682640372604, \ \gamma_2 = -0.00015911724084755207863, \ \omega = 1.5006859732648583225.$$

We remark that this analytical expression permits to describe precisely, up to time $t = 80$, the behavior of the first mode that is simulated and also the whole electric energy, as this first mode is dominant. For the simulation, we have used the BSL method on a 1024×2048 grid, with $\Delta t = 0.1$. The study of the linear analysis at order 2 developed in Subsection 3.2 permits to explain the behavior of the electric energy up to time $t = 90$, and the behavior of the second Fourier mode from initial time to time $t = 90$. We have used here the following analytical expression for the second Fourier mode

$$\mathcal{E}_2 = A^2 \left(0.3 \exp(2 \cdot 0.089t) + 0.7 \exp(0.145t) \right). \tag{20}$$

Here the coefficients 0.3 and 0.7 are chosen to fit the numerical results, 0.089 is an approximation of γ_1 and 0.145 is the rounding of 0.144982725814, coming from the dispersion analysis of 3.2. The theoretical electric energy is then given in the figures by $\sqrt{\mathcal{E}_1^2 + \mathcal{E}_2^2}$. Note that after time 100, we are in the non linear phase and the dispersion relation analysis is no more valid.

On Figure 5, we take $A = 0.01$, as in [18]. We take here as parameters, the BSL method on a grid 128×256 with $\Delta t = 0.02$. The behavior is similar. As the perturbation is bigger, the non linear phase appears sooner. We can note also that the first mode does not have time to develop and that the instability is essentially explained by the second order expansion.

Then, we study the influence of the numerical parameters, on Figure 6. We see that for $A = 0.0001$, the grid 64×256 is quite good, as the difference with the refined run on a grid 1024×2048 (similar to 2048×4096) is only visible at the end of the simulation, around $T = 150$. For $A = 0.01$, we get converged results until T around $80 - 100$; then for longer times, we see that the results start to differ, and the grid 64×256 seems not fine enough. For the time step, it seems that $\Delta t = 0.1$ is a good choice, as the results are very similar between $\Delta t = 0.02$ or $\Delta t = 0.1$.

On Figures 13, 14, 15, 16, we can appreciate the convergence on the diagnostics of conservation of L^1, L^2 norms; the mass is conserved up to machine precision.

$x - vx$ cut permits to measure the structures and the filaments, here for $A = 0.01$. It is confirmed that at time $T = 80$, the mesh 64×256 correctly describes the ions (see Figures 11 and 12). At time $T = 150$, however, as already seen on the electric energy (Figure 6 right), we see the differences between the fine run (512×2048 grid) and the coarse one (64×256) for the ions (see Figures 9 and 10); for the electrons the differences are smaller.
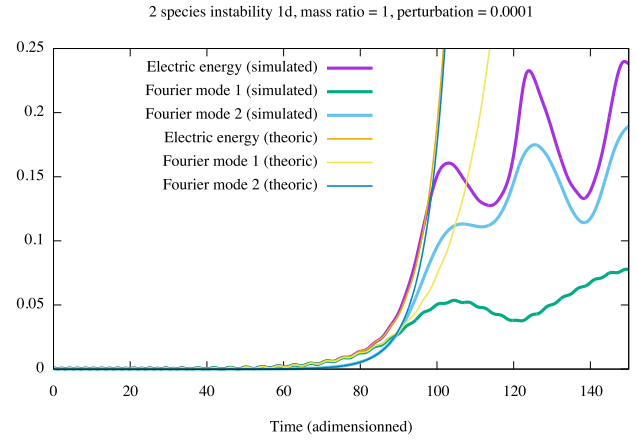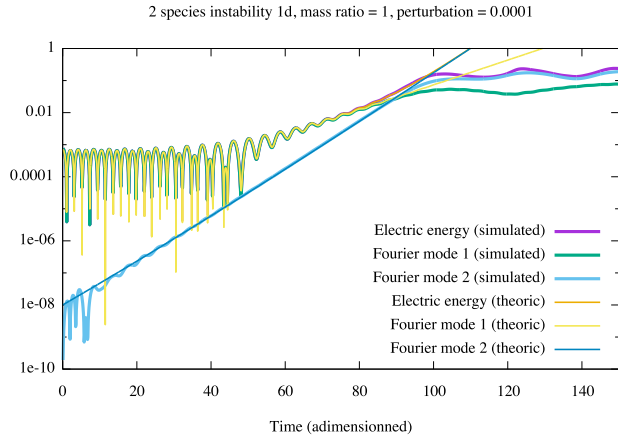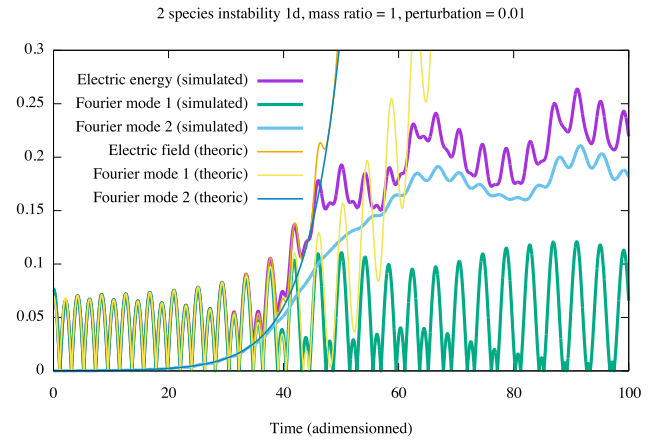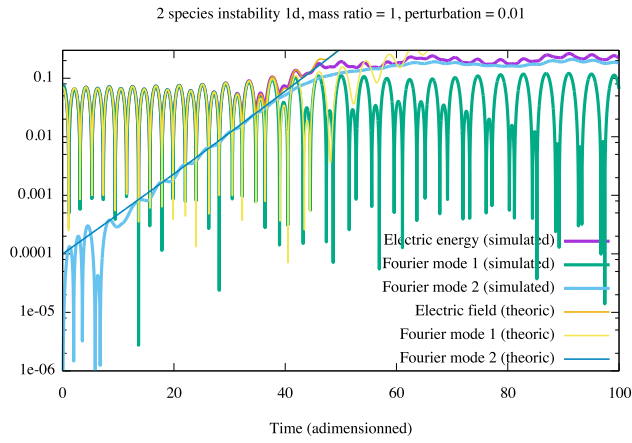
Figure 4: $A = 0.0001$ First test case
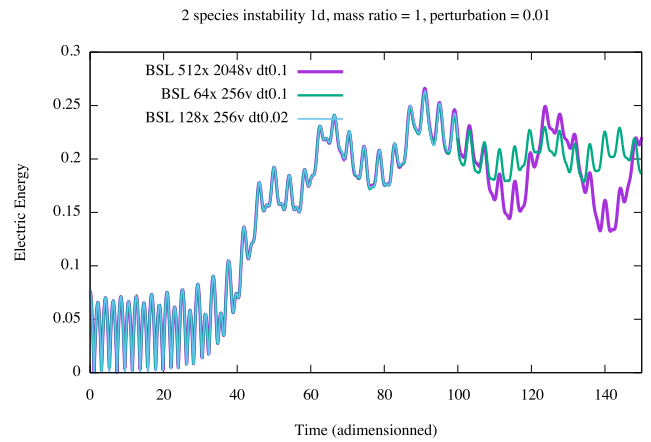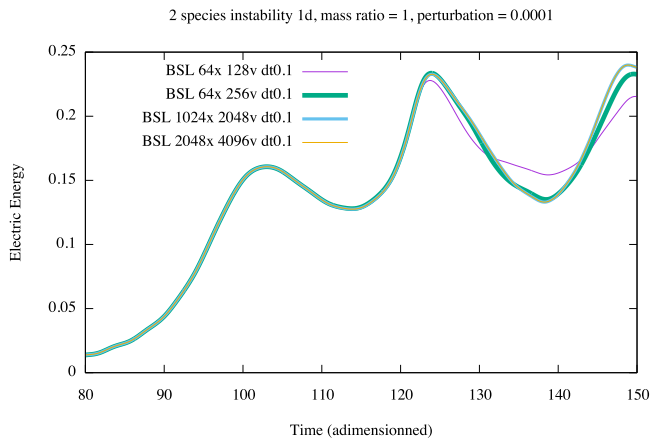

Figure 5: $A = 0.01$ First test case

Figure 6: Convergence study of the electric energy for the first test case: $A = 0.0001$ (left) and $A = 0.01$ (right)
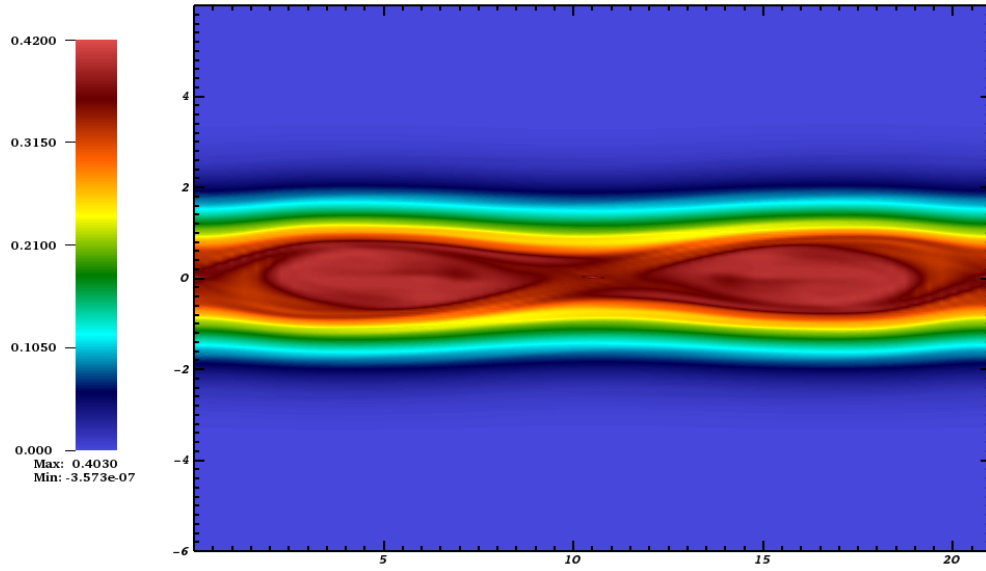
Figure 7: $x - vx$ cut for first test case (electrons distribution) for $A = 0.01$ on 64×256 grid, at time $T = 150$
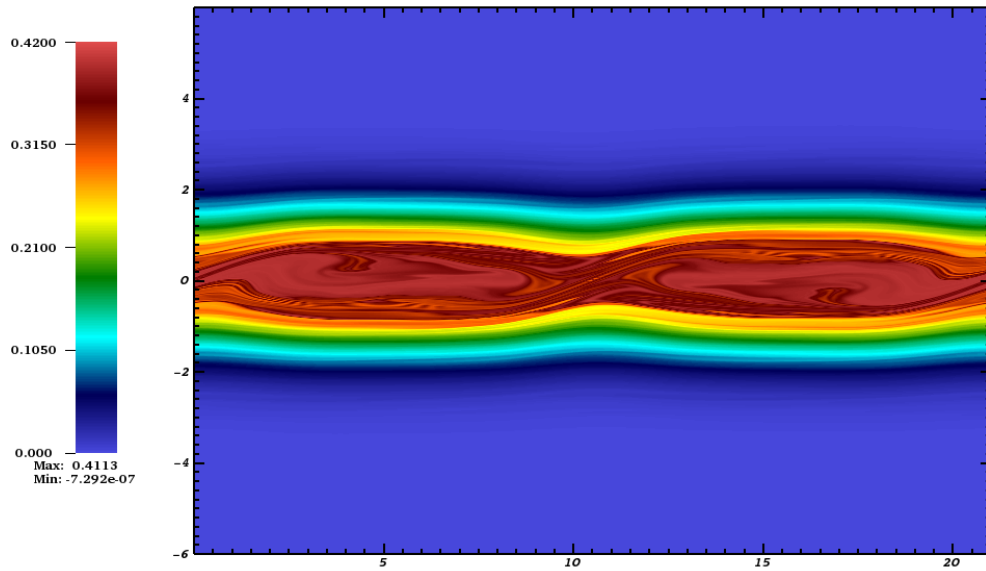

Figure 8: $x - vx$ cut for first test case (electrons distribution) for $A = 0.01$, BSL $\Delta t = 0.1$ on 512×2048 grid, at time $T = 150$
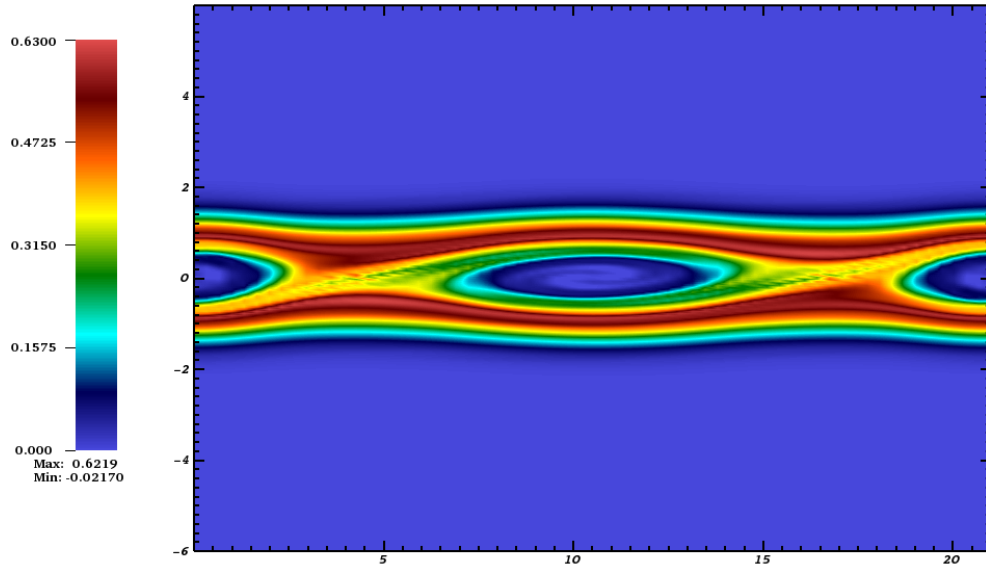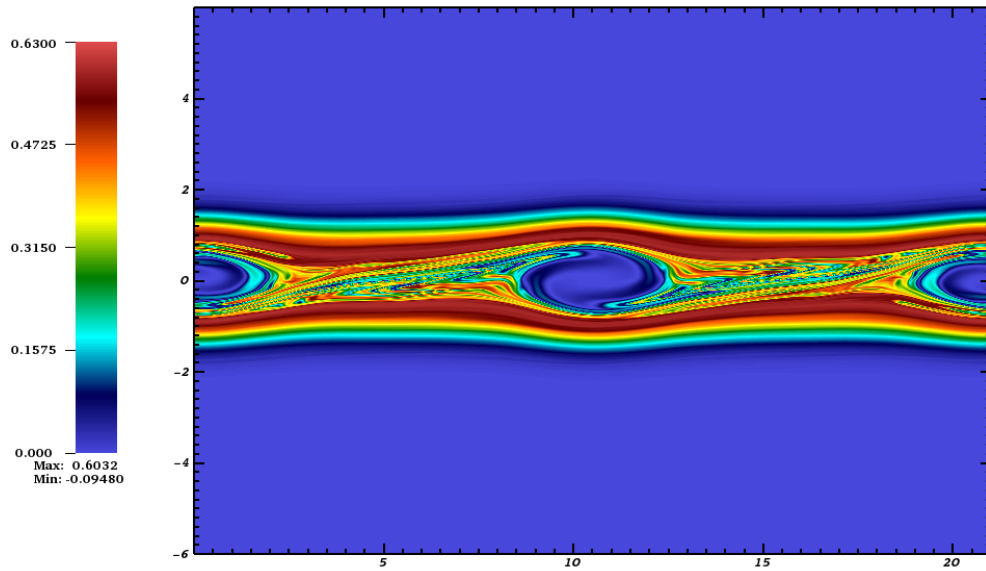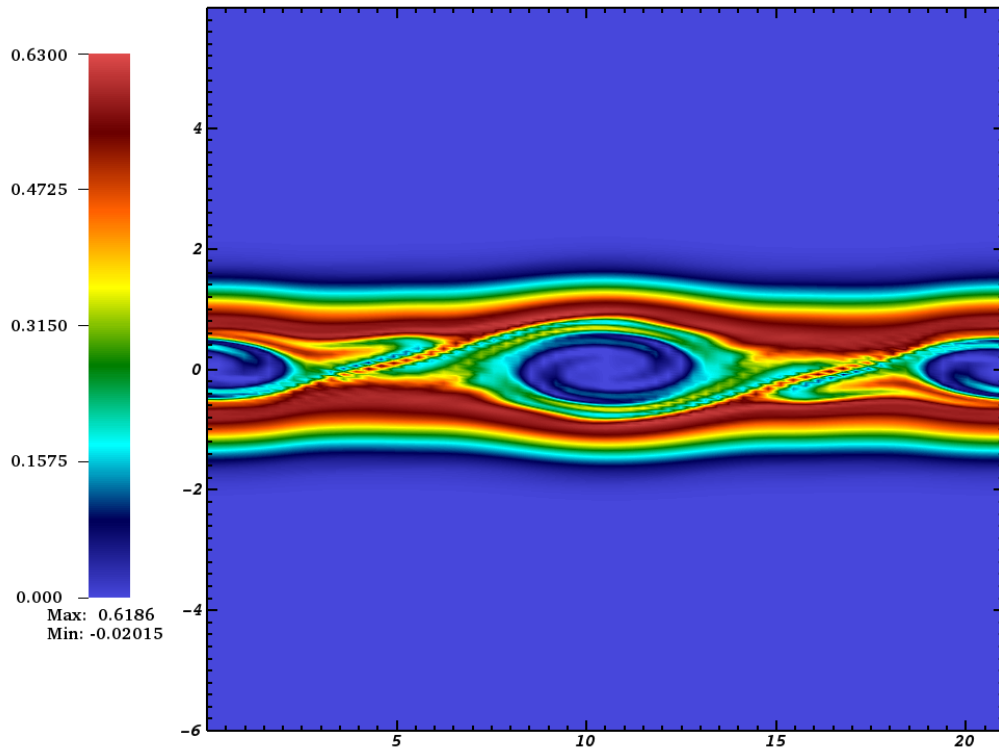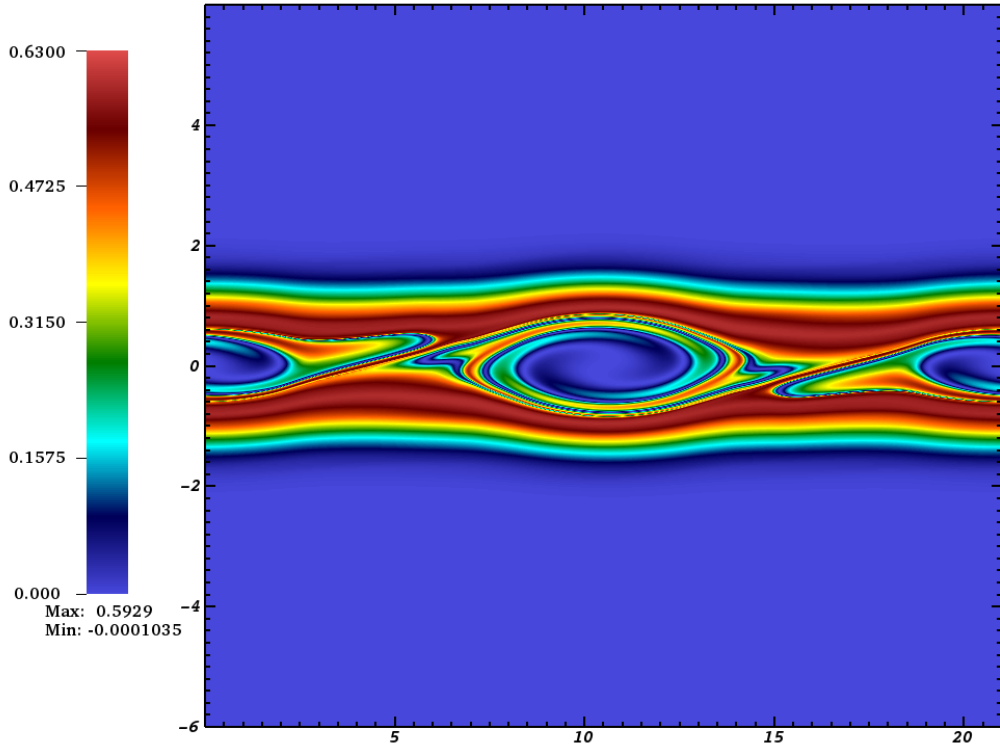
13

Figure 9: $x - vx$ cut for first test case (ions distribution) for $A = 0.01$ on 64×256 grid, at time $T = 150$

Figure 10: $x - vx$ cut for first test case (ions distribution) for $A = 0.01$, BSL $\Delta t = 0.1$ on 512×2048 grid, at time $T = 150$

14

Figure 11: $x - vx$ cut for first test case (ions distribution) for $A = 0.01$ on 64×256 grid, at time $T = 80$

Figure 12: $x - vx$ cut for first test case (ions distribution) for $A = 0.01$, BSL $\Delta t = 0.1$ on 512×2048 grid, at time $T = 80$
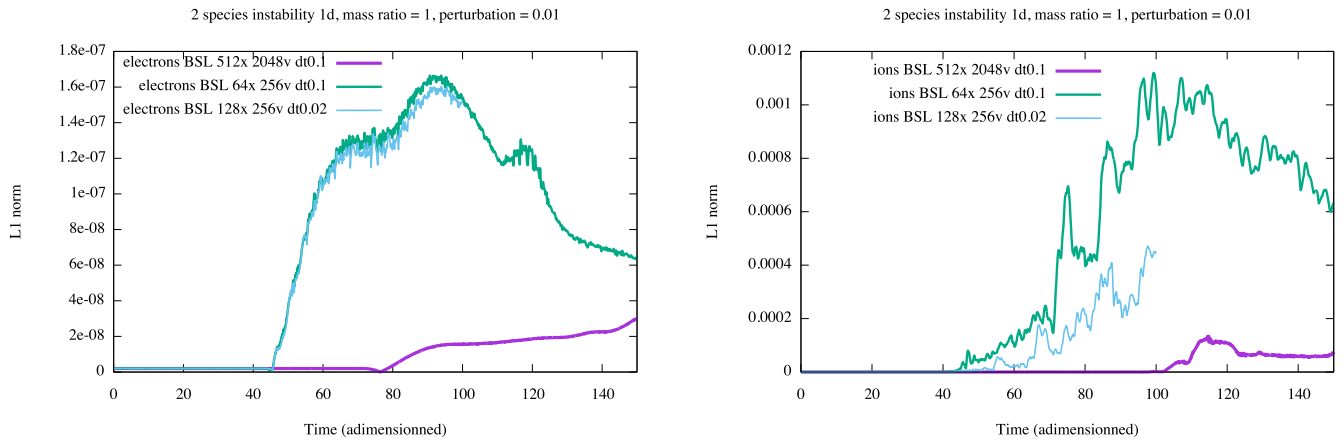
Figure 13: Relative error of L^1 norm, $A = 0.01$, first test case
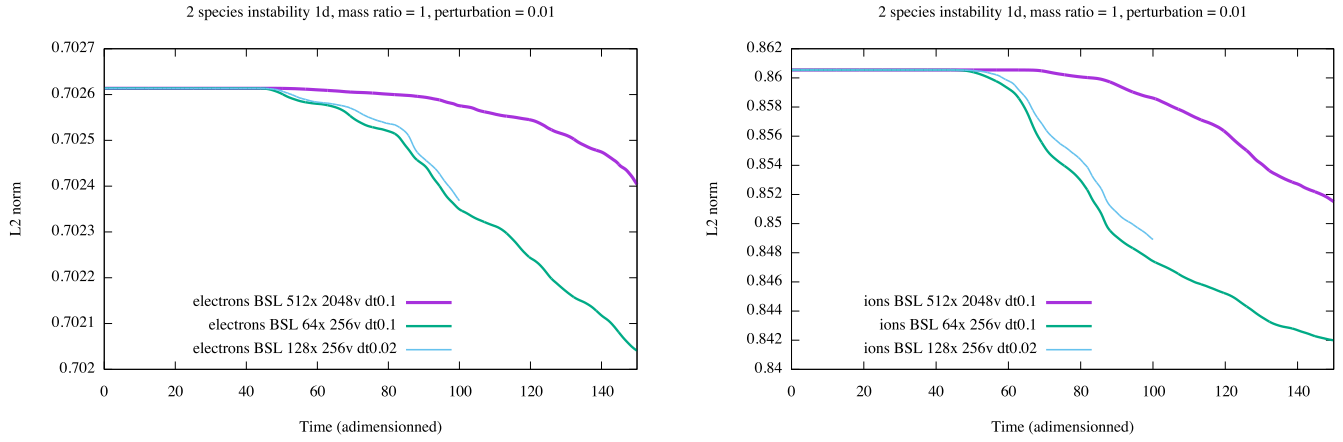
Figure 14: L^2 norm, $A = 0.01$, first test case
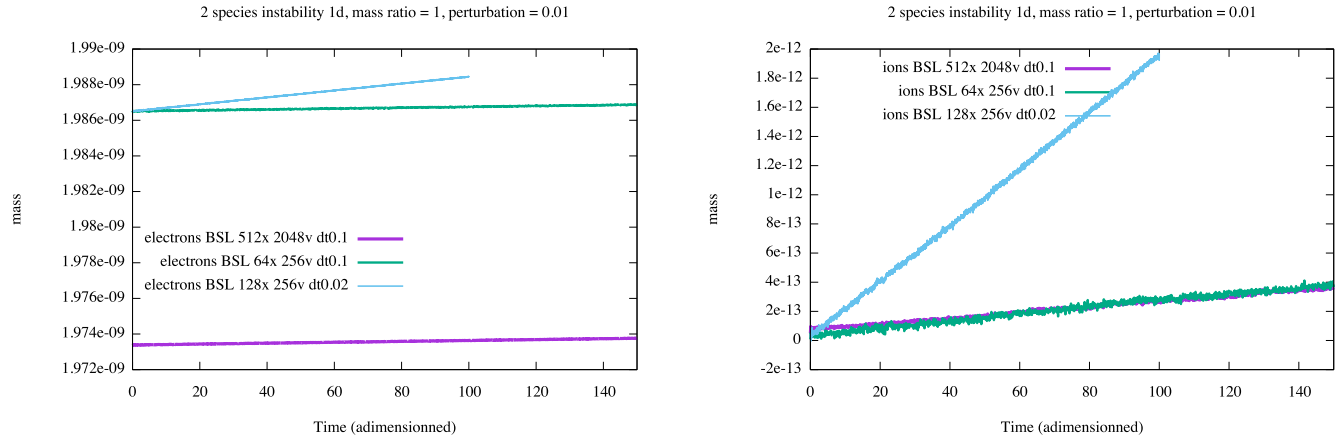
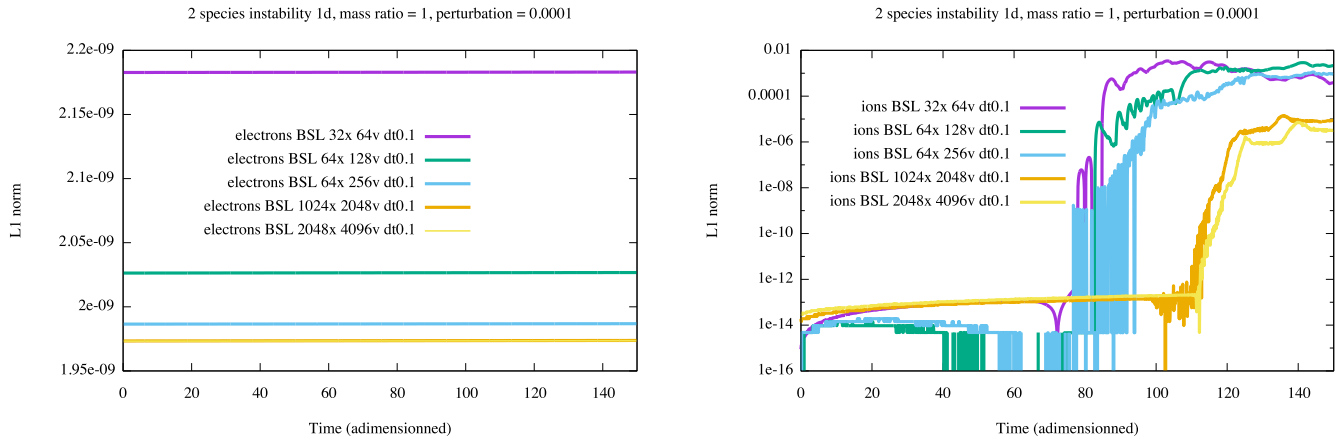Figure 15: Relative mass error, $A = 0.01$, first test case

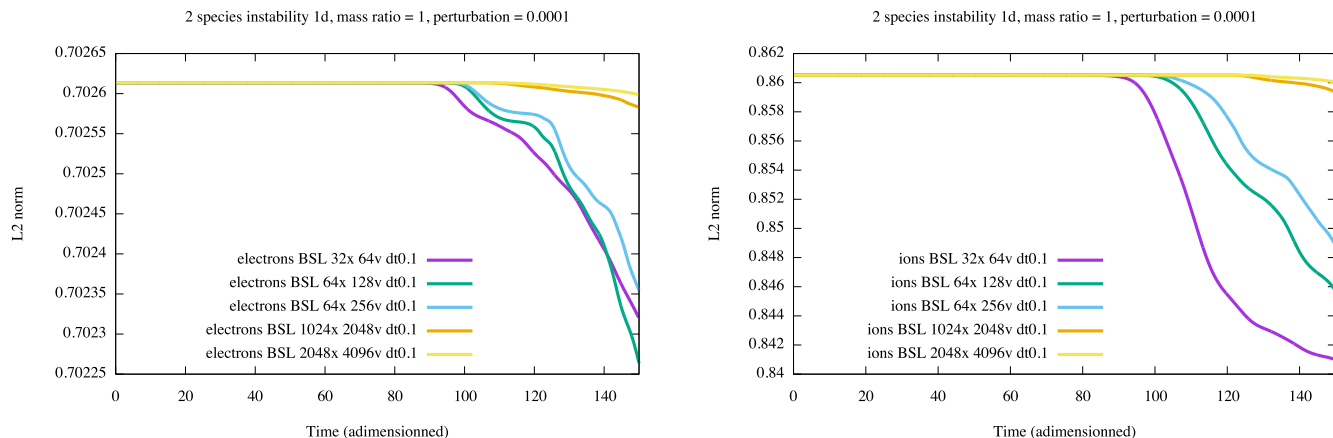Figure 16: Relative error of L^1 norm, $A = 0.0001$, first test case

Figure 17: L^2 norm, $A = 0.0001$, first test case

5.2 Second test case: $2D \times 2D$ one-species

This test case is described in Subsection 2.2.

On Figure 18 (left, logarithmic scale; right, standard scale), we represent, for the perturbation $A = 0.1$, the electric energy defined by $\sqrt{\frac{1}{2} \int_0^L |E|^2 dx}$ versus time t and also the absolute value of the first and second Fourier modes multiplied by $\sqrt{\frac{1}{2}}$, in order to be comparable to the electric energy. We represent also *theoretical* results, coming from the study of the dispersion analysis developed in Section 3. The theoretical first mode is here the expression

$$\mathcal{E}_1 = 0.89 \left| \cos(1.416t + 2.6) \exp(-0.1533x) \right| . \tag{21}$$

We have here only used the theoretical values 1.416, -0.1533 and fitted the two other coefficients.

We remark that this analytical expression permits to describe precisely, up to time $t = 12$, the behavior of the first mode that is simulated and also the whole electric energy, as this first mode is dominant. For the simulation, we have used the BSL method on a $32 \times 32 \times 256 \times 256$ grid, with $\Delta t = 0.1$. The study of the linear analysis at order 2 developed in Subsection 3.2 permits to explain the behavior of the electric energy up to time $t = 25$, and the behavior of the second Fourier mode from initial time to time $t = 25$. We have used here the following analytical expression for the second Fourier mode

$$\mathcal{E}_2 = 0.0028 \exp(0.259t) \tag{22}$$

Here the coefficients 0.0028 is chosen to fit the numerical results, 0.259 is coming from the dispersion analysis of 3.2. The theoretical electric energy is then given in the figures by $\sqrt{\mathcal{E}_1^2 + \mathcal{E}_2^2}$. Note that after time $25 - 30$, we are in the non linear phase and the dispersion relation analysis is no more valid.

We then study the convergence on the diagnostic of the electric energy on Figures 19 and 20 (left). We notice that both PIC and BSL methods converge to the same state in the non linear phase, which permits to validate the results, from this cross comparison.

We see on Figure 20 (right) the time evolution of the L^2 norm; we notice that the conservation is clearly improved by refining the grid in space.

On Figures 21 and 22, we see $x - vx$ and $y - vy$ cuts; the first looks similar to two-stream instability and the second to Landau damping simulations. The filaments seem to be well resolved thanks to a relatively high number of points in the velocity directions.

On Figure 23, we see the contour plots of ρ at different times; we clearly see the behavior of the modes: first the mode $(0, 1)$ dominates and then it is the mode $(1, 0)$.
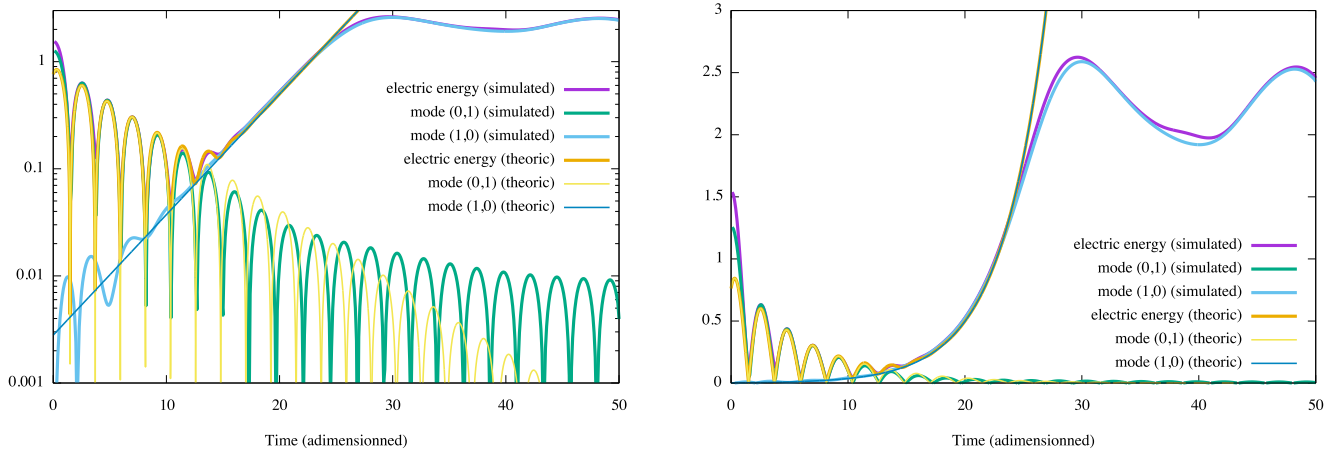
Figure 18: Comparison between simulation and analytical results from dispersion relation, on the electric energy and the relevant modes. $A = 0.1$, second test case
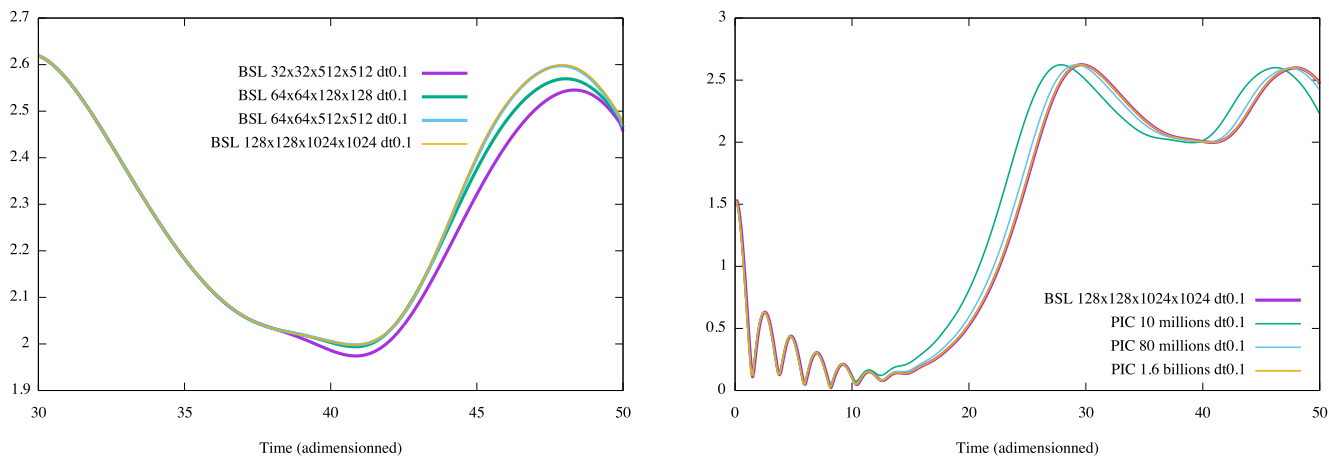

Figure 19: Time evolution of electric energy, with convergence of BSL (left) and PIC (right). $A = 0.1$, second test case. Different grid sizes for BSL and different numbers of particle for PIC are used. Time step is $\Delta t = 0.1$. The reference solution is here BSL with grid size $128 \times 128 \times 1024 \times 1024$.
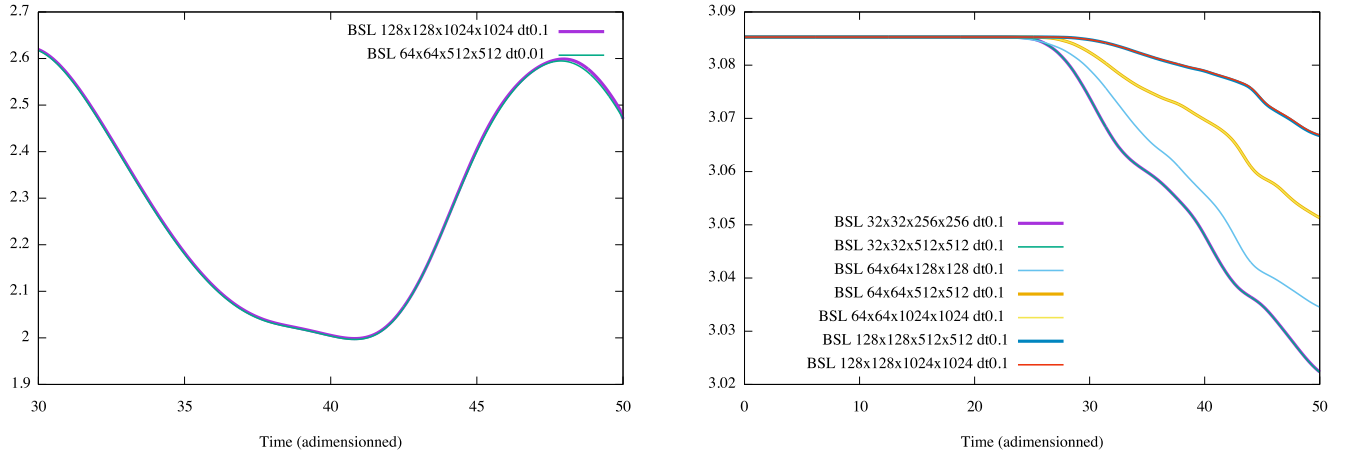
Figure 20: Left: time evolution of electric energy with convergence in time for BSL. The solution with BSL with grid size $128 \times 128 \times 1024 \times 1024$ and $\Delta t = 0.1$ is similar to the solution with $64 \times 64 \times 512 \times 512$ and $\Delta t = 0.1$, which is also similar to the solution with $64 \times 64 \times 512 \times 512$ and $\Delta t = 0.01$. Right: time evolution of L^2 norm of f. Second test case, with $A = 0.1$.
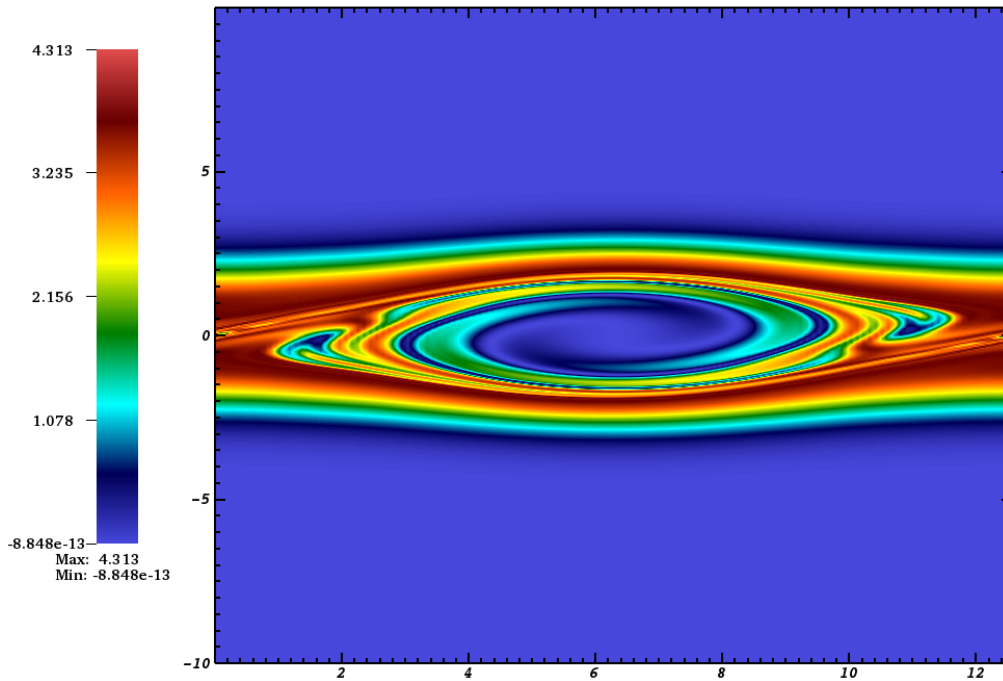

Figure 21: $x - vx$ cut for second test case for $A = 0.1$; BSL $128 \times 128 \times 1024 \times 1024$, $\Delta t = 0.05$ at final time $t = 50$.
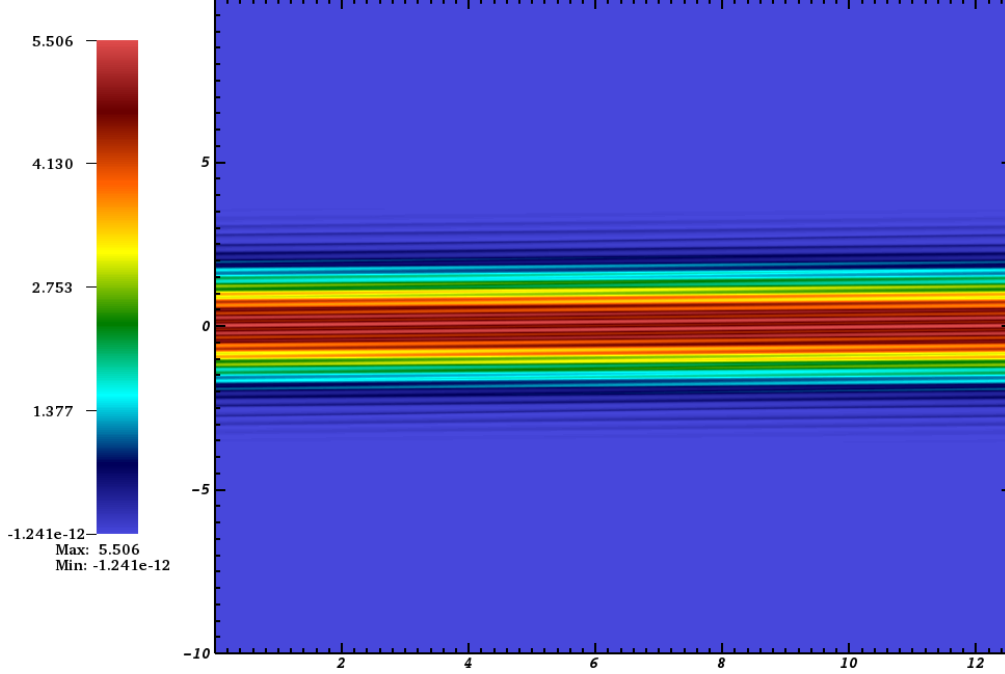
20

Figure 22: $y - vy$ cut for second test case for $A = 0.1$; BSL $128 \times 128 \times 1024 \times 1024$, $\Delta t = 0.05$ at final time $t = 50$.

5.3 Third test case: $2D \times 2D$ two-species

This test case is described in Subsection 2.3. We take here $\varepsilon = 0.01$. This leads to a more oscillatory behavior. We focus here on the electric energy. On Figure 24, we give the electric energy for BSL using the 6-th order scheme, for $\Delta t = 0.02$ and $\Delta t = 0.01$. We remark that there is a lot of oscillations. We see that the results are very similar, which is a mark of the fact that the scheme is converged in time. We then do the comparison with other methods and numerical parameters. The same quantity is plotted for other numerical parameters on Figures 25, 26, 27, 28, 29.
On Figure 25, we see that the result is equivalent with using the Strang scheme with $\Delta t = 0.0025$.
On Figure 26, we see that the convergence is not complete when passing from a grid $32 \times 256 \times 32 \times 512$ to a grid $32 \times 512 \times 32 \times 1024$, which means that high resolution in $y - vy$ is needed.
On Figure 27, we see that on the contrary, 32 points in x seem sufficient, as the curve for the $32 \times 512 \times 32 \times 1024$ and $64 \times 512 \times 32 \times 1024$ well match, and we see that going to $\Delta t = 0.005$ in the Strang splitting case changes more the solution; so that it seems to be a little better to stick to $\Delta t = 0.0025$.
On Figure 28, we see that more clearly that high resolution in $y - vy$ is needed: the grid 128 in y and 512 in v_y is clearly not sufficient.
On Figure 29, we see simulations using a splitting first by species. The time step for the ions is $\Delta t_i = 0.1$; for the electrons the time step is $\Delta t_e = 0.01$; BSL (resp. PIC) is used for the electrons on the left (resp. right) figure. The results are converged (they are compared to a "reference" solution: BSL with 6-th order time scheme and $\Delta t = 0.01$ on grid $32 \times 512 \times 32 \times 2048$). Thus, we validate the splitting by species using BSL for ions and BSL or PIC for electrons, with sub-steps for the electrons. This opens the door to use specific PIC (or BSL) schemes that are designed for capturing high oscillations (see [8]). On Figure 30, we compare the total energy conservation between Strang and the 6-th order splitting; we remark that the conservation is really improved with the 6-th order splitting, which is coherent with [7], where such a splitting is also used for a single species. Then, on Figures 31, 32, 33, 34, 35, we give some $2D$ plots.
On Figure 31, we see the $x - vx$ cut for the electrons (left) and the ions (right). We note that this picture does not change much with time; in particular, luckily, a two-stream instability is here not developed, which permit to keep a resolution small in these directions.
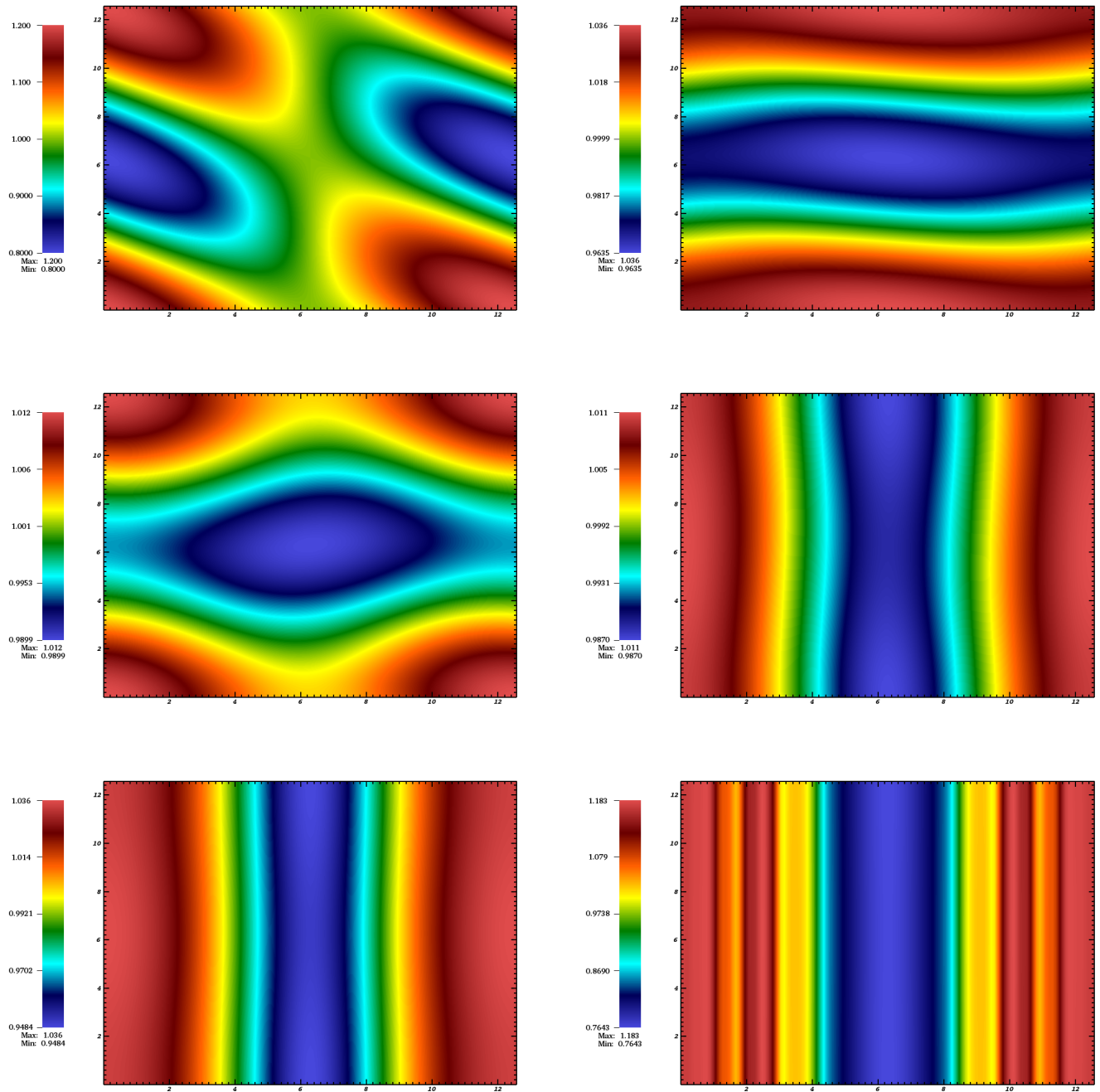
Figure 23: ρ at different times ($t = 0, 5, 10, 15, 20, 50$); BSL $128 \times 128 \times 1024 \times 1024$, $\Delta t = 0.05$; second test case, $A = 0.1$
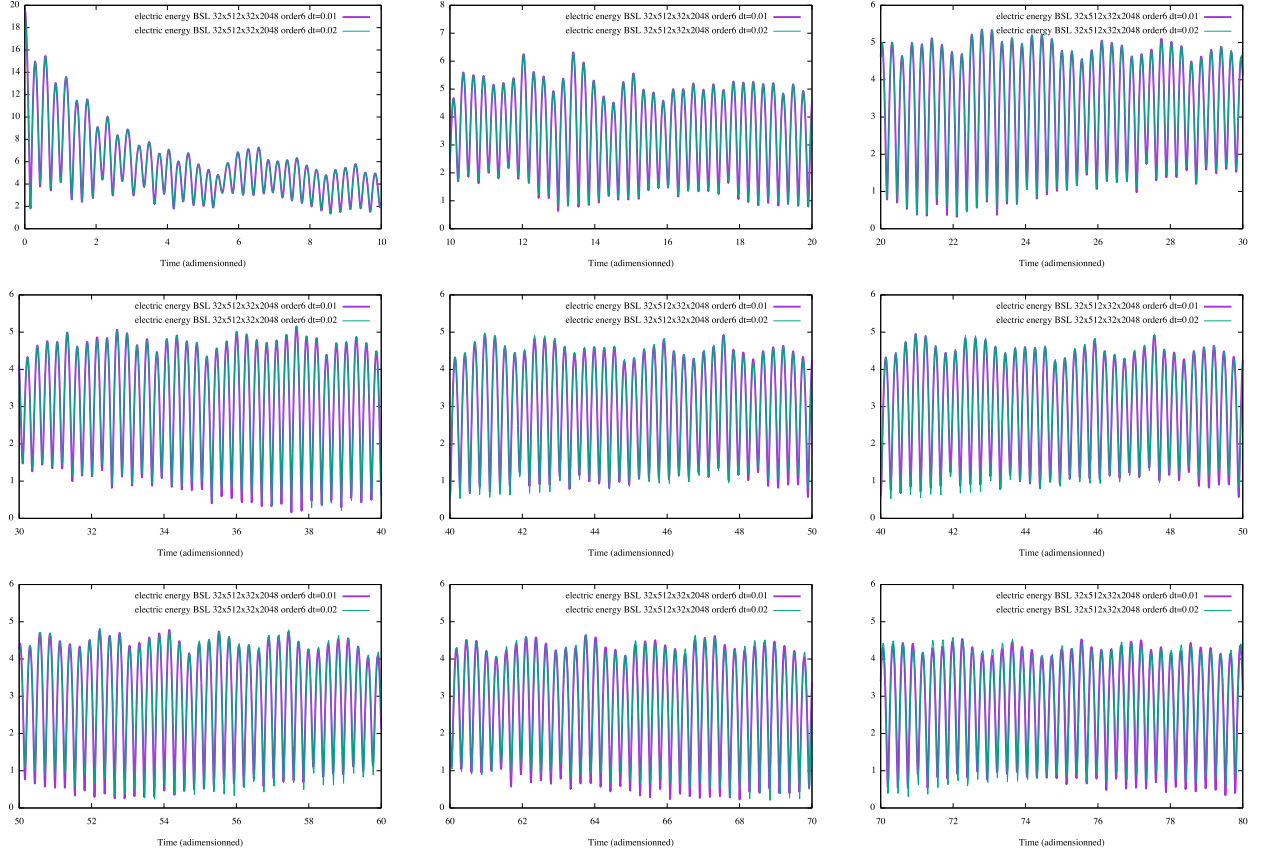
Figure 24: Electric energy, third test case: comparisons for 6-th order scheme and $\Delta t = 0.01$ vs $\Delta t = 0.02$, on $32 \times 512 \times 32 \times 2048$ grid with BSL

On Figure 32, we see on the contrary, that for the $y - vy$ cut for the electrons, very fine structures appear; this confirms the fact that high resolution is here needed.

On Figure 33, we see a Landau damping behavior in for the $y - vy$ cut for the ions.

On Figure 34, we see the time evolution of $\rho_e = \int f_e(x, y, v_x, v_y)dv_xdv_y$, and on Figure 35, the time evolution of $\rho_i = \int f_i(x, y, v_x, v_y)dv_xdv_y$. We see the rapid change of ρ_e with respect to time; we remark also some structures in x and the amplitude of $\rho - 1$ is small.

6 Efficiency results

We present below the time needed to achieve the simulations shown in this paper, along with strong scaling results of our code on the second test case, for both the PIC method and the BSL method. All the experiments were run on the supercomputer Curie[3]: 5,040 nodes, each node has 2 sockets, each socket being a Intel Xeon E5-2680 @2.7 GHz (SandyBridge), with 64 GB of RAM, 4 memory channels and 8 cores. The code is compiled with `ifort` 16.0.3.210 from Intel.

For the BSL method, we show efficiency as the number of cells updated by second. It can be computed by the following formula :

$$\frac{ncx \times ncy \times ncvx \times ncvy \times num\_iteration \times num\_split\_step \times 2}{num\_processes \times execution\_time}$$

where $ncx \times ncy \times ncvx \times ncvy$ are the grid sizes, $num\_iteration$ is the number of time iterations, num_split_step is the number of steps of the time splitting (3 for the Strang splitting, 23 for the classical 6th order splitting), and 2 because each $2D$ advection is split as two $1D$ advections.

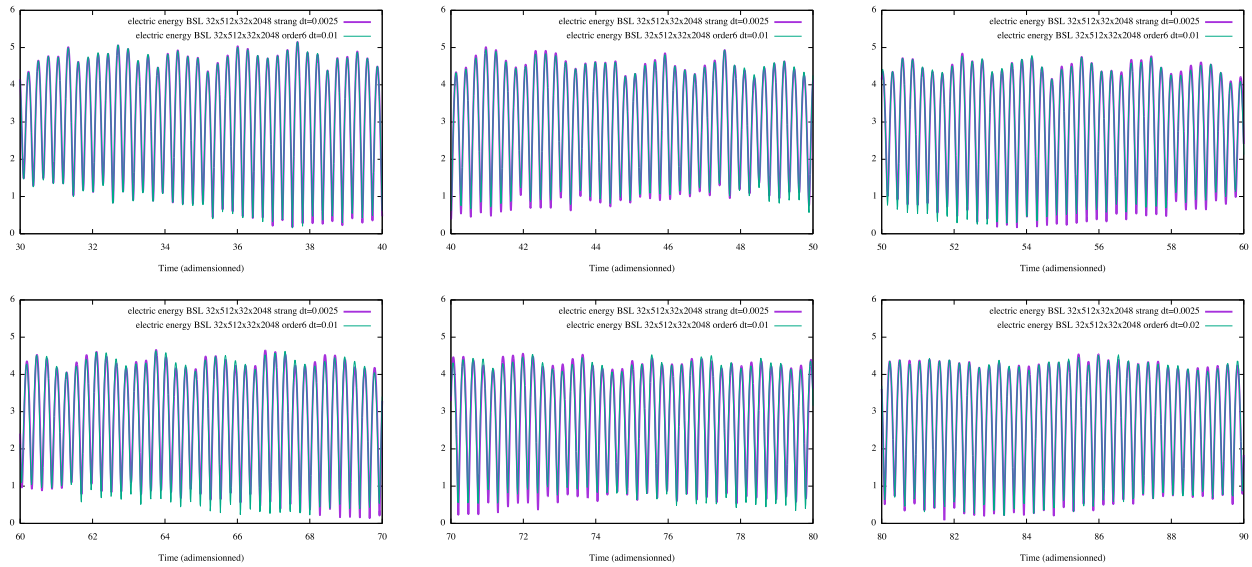[3]http://www-hpc.cea.fr/fr/complexe/tgcc-curie.htm

Figure 25: Electric energy, third test case: comparisons for 6-th order splitting and $\Delta t = 0.01$ (or $\Delta t = 0.02$) Strang splitting with $\Delta t = 0.0025$, on $32 \times 512 \times 32 \times 2048$ grid with BSL
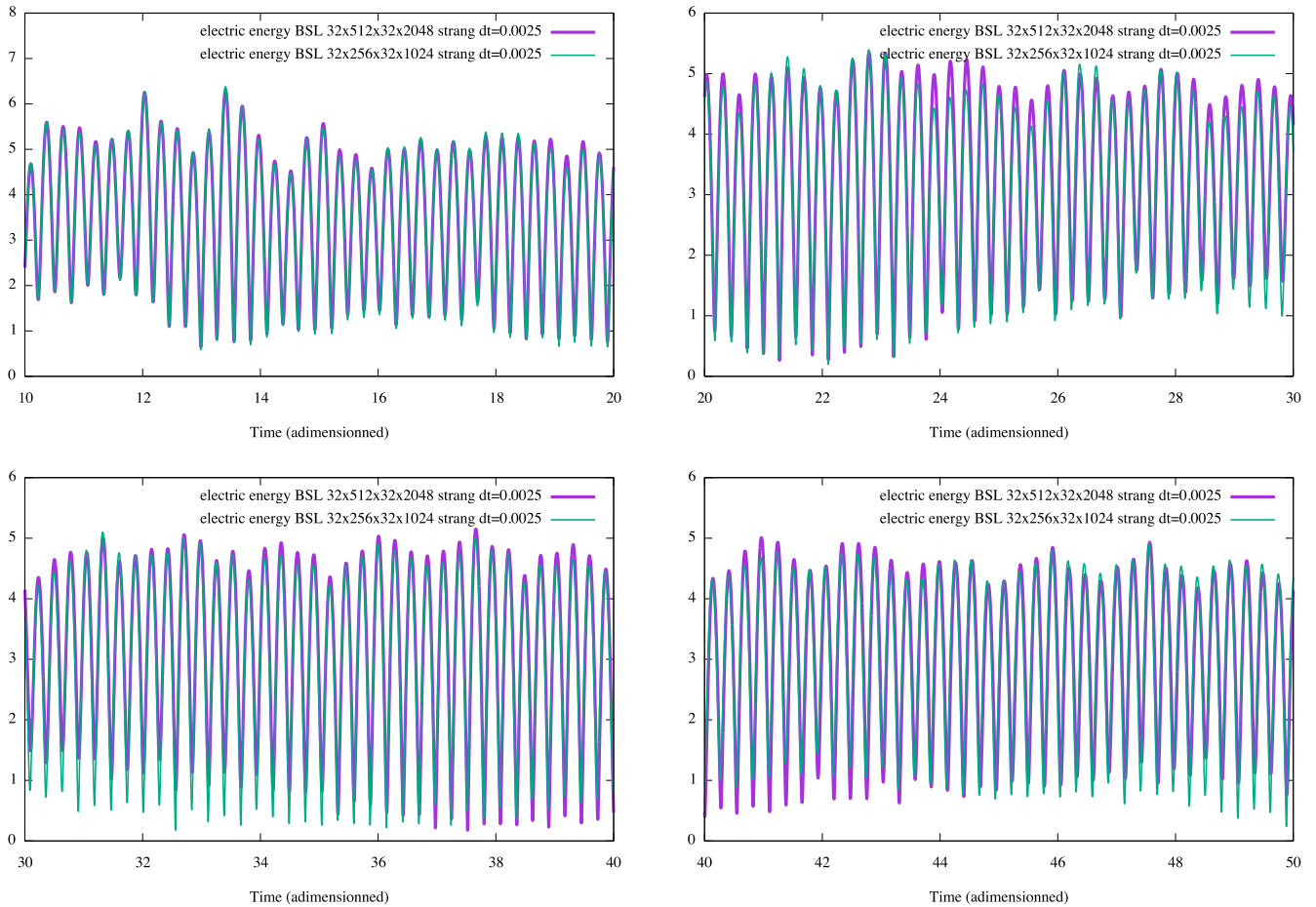

Figure 26: Electric energy, third test case: comparisons between $32 \times 512 \times 32 \times 2048$ grid and $32 \times 256 \times 32 \times 1024$ grid with BSL, using Strang splitting with $\Delta t = 0.0025$
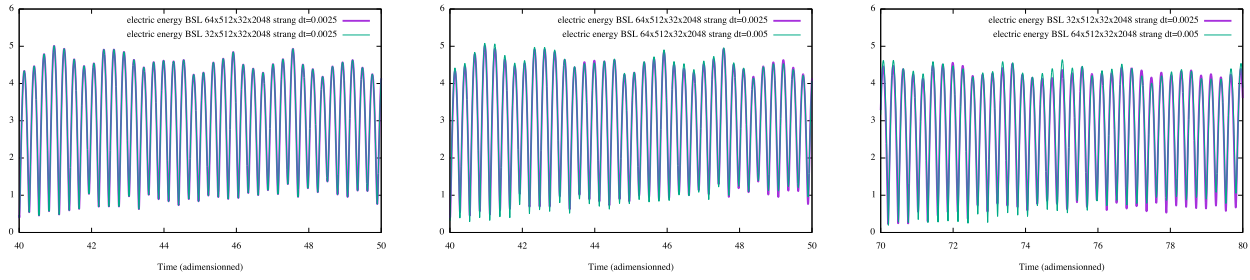
24

Figure 27: Electric energy, third test case: comparisons between grids $32 \times 512 \times 32 \times 2048$ and $64 \times 512 \times 32 \times 2048$, with Strang splitting and $\Delta t = 0.005$ or $\Delta t = 0.0025$
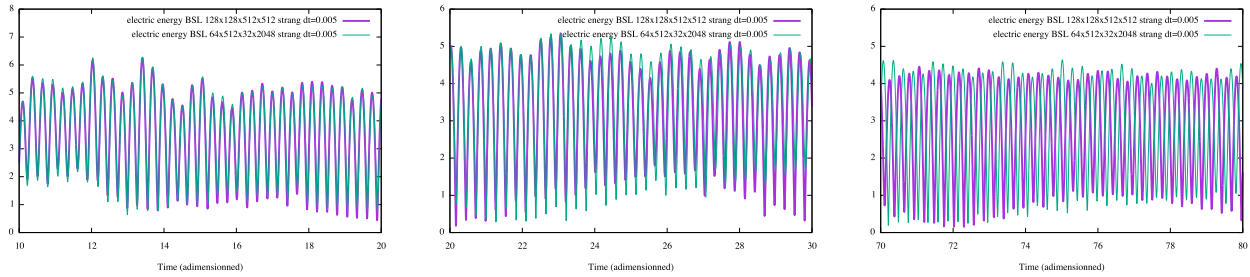

Figure 28: Electric energy, third test case: comparisons between $64 \times 512 \times 32 \times 2048$ grid and $128 \times 128 \times 512 \times 512$ grid with BSL, using Strang splitting with $\Delta t = 0.005$
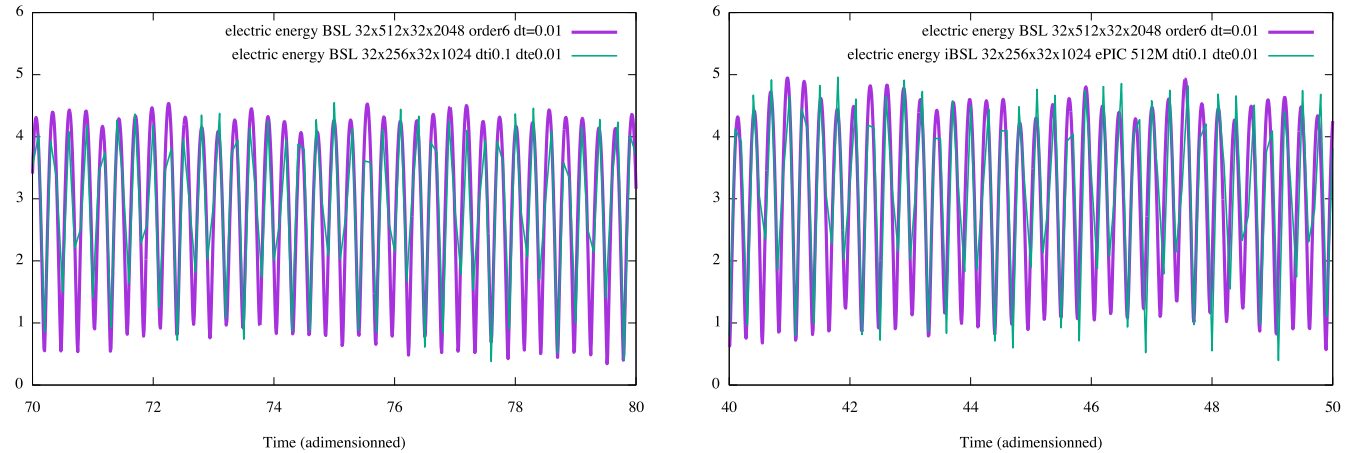
Figure 29: Electric energy, third test case; splitting first by species $\Delta t_{\text{ions}} = 0.1$, $\Delta t_{\text{electrons}} = 0.01$ (for the ions: BSL; for the electrons: BSL, left; PIC right), on grid $32 \times 512 \times 32 \times 2048$
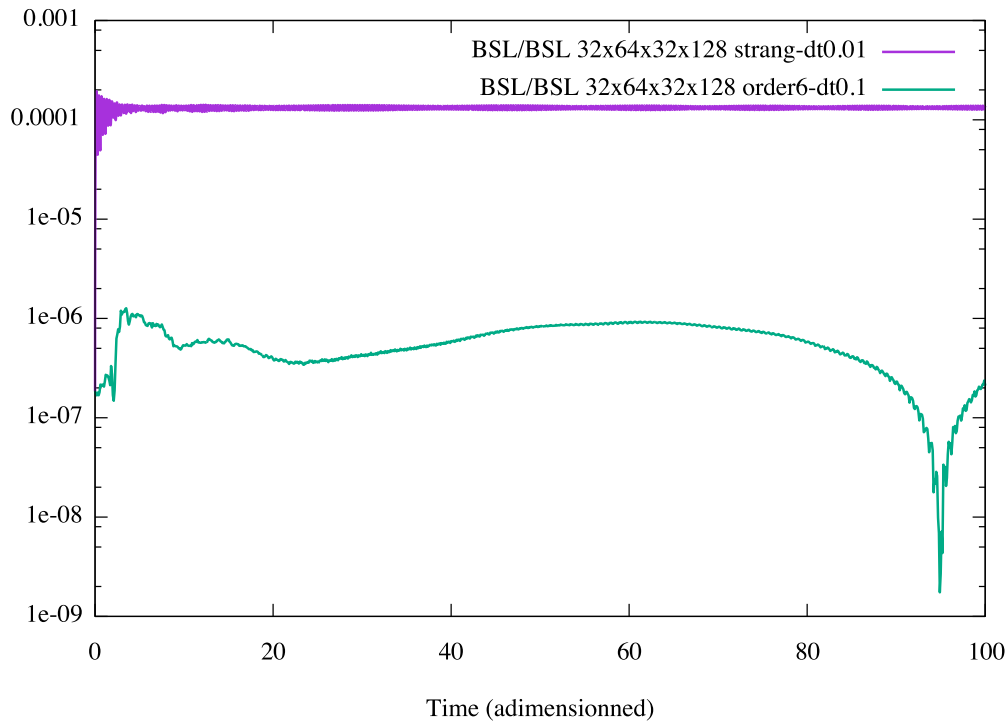
Figure 30: Total energy, third test case: comparison between order 6, with $\Delta t = 0.1$ and Strang, with $\Delta t = 0.01$ on $32 \times 64 \times 32 \times 128$ grid, with BSL

Figure 31: x-vx cut electrons (left) and ions (right), third test case

Figure 32: y-vy cut electrons at times $2, 4, 5, 10, 20, 50$, third test case

Figure 33: y-vy cut ions at times $10, 20, 50, 100$, third test case

Figure 34: ρ for electrons at time $44.3, 44.4$, third test case

28

Figure 35: ρ for ions at time $50, 54$, third test case

6.1 Test case 1

The first test case can be simulated very fast, as it is only $1D \times 1D$. However, our code being designed for $2D \times 2D$, we took 4 points in the y and the vy di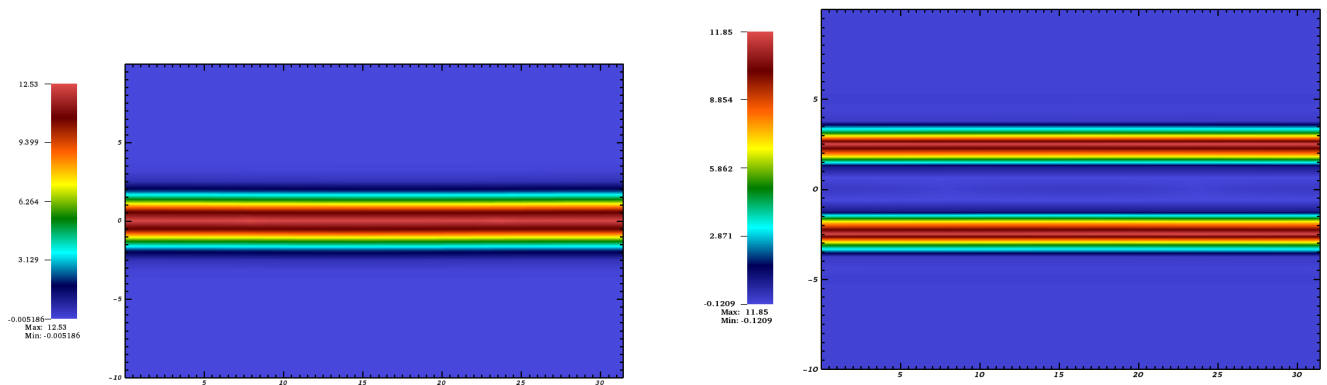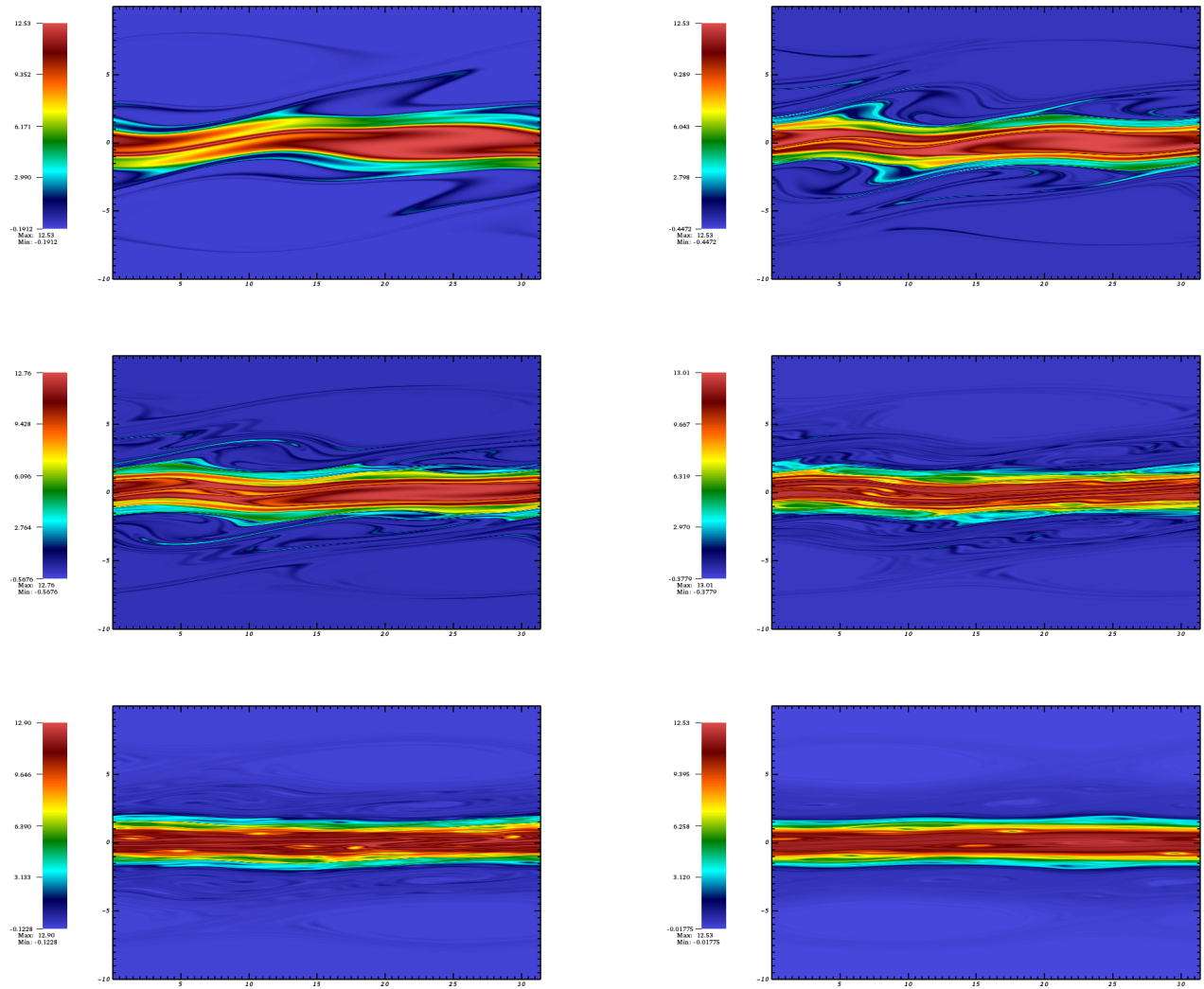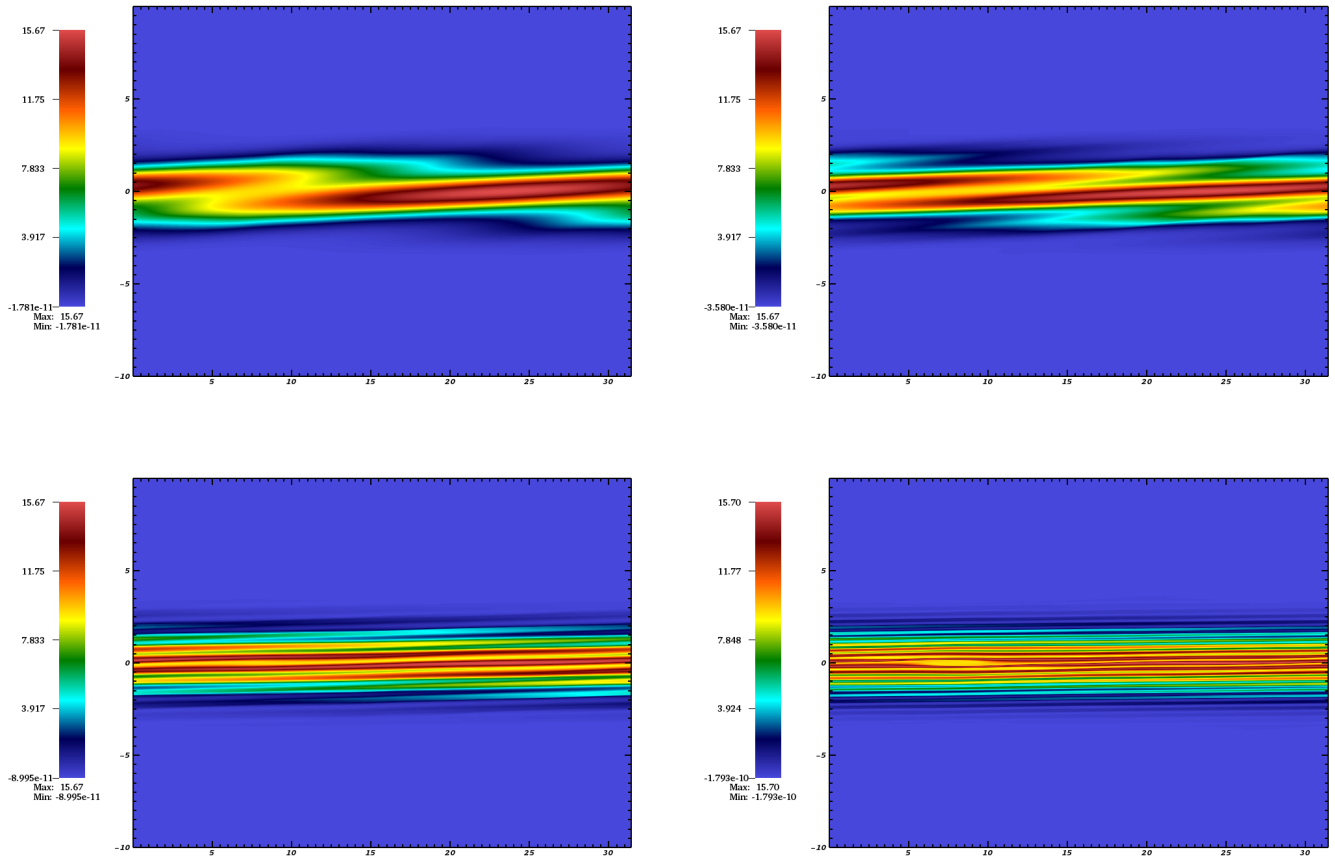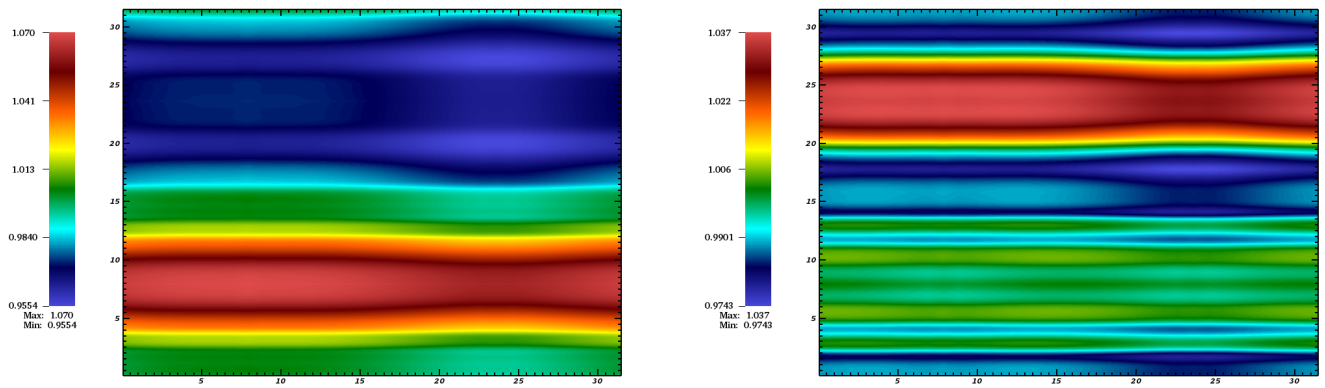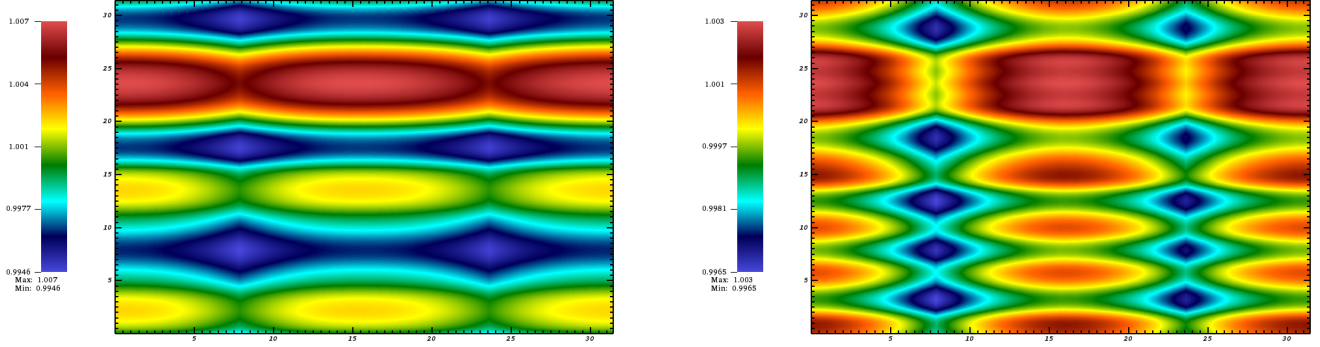rections, with uniform distribution across those directions. Execution time and efficiency (in millions of cells updated per second per processor) for each discretization are shown in Table 1.

Table 1: Time spent in the simulation, first test case.

ncx	$ncvx$	$num\_iteration$	MPI processes	Execution time	Computing time	Efficiency
128	256	1500	32	36.7 s	1176 s	4.01
512	2048	1500	32	1107 s	1 h	4.26
512	2048	3000	32	2214 s	20 h	4.26
64	128	1500	32	11.9 s	381 s	3.09
64	256	1500	32	25.8 s	826 s	2.86
1024	2048	1500	512	291 s	41 h	2.03
2048	4096	1500	1024	701 s	200 h	1.68

Top : perturbation $= 0.01$; bottom : perturbation $= 0.0001$.

6.2 Test case 2

For the second test case, execution time and efficiency (in millions of cells updated per second per processor) for each discretization are shown in Table 2.

Table 2: Time spent in the simulation, second test case.

ncx	ncy	$ncvx$	$ncvy$	$num\_iteration$	MPI processes	Execution time	Computing time	Efficiency
32	32	256	256	500	32	511 s	4.5 h	12.3
32	32	512	512	500	128	508 s	18 h	12.4
64	64	128	128	500	32	429 s	3.7 h	15.0
64	64	512	512	500	256	868 s	62 h	14.5
64	64	1024	1024	500	1024	1134 s	13 days	11.1
128	128	512	512	500	1024	893 s	10.5 days	14.1
128	128	1024	1024	500	4096	1427 s	67.5 days	8.8

The scalability of our code was tested using this test case. Results for the BSL code are shown in Figure 36, for the $64 \times 64 \times 512 \times 512$ grid size (minimum grid size needed for convergence).

What can be seen in this figure, as well as in the previous tables, could be predicted. As long as there is enough computations to do for each processor, the code is efficient. As soon as the number of cells per processor is too low, the communications become a bottleneck, and the efficiency is lowered.
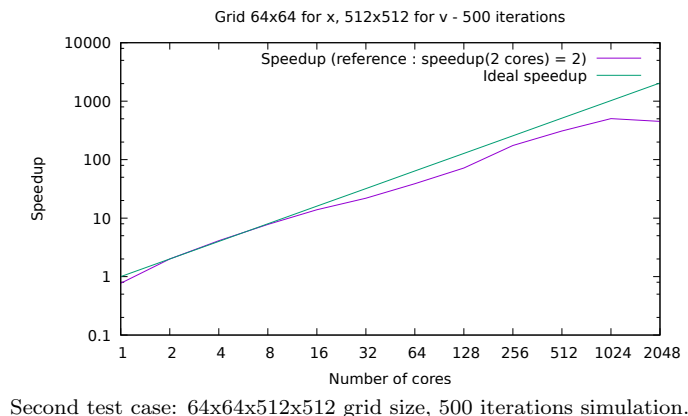
29

Grid 64x64 for x, 512x512 for v - 500 iterations

Second test case: 64x64x512x512 grid size, 500 iterations simulation.

Figure 36: Strong scaling on Curie : Pure MPI.

Results for the PIC code are shown in Figure 37, for 800 million particles with a 128×128 grid size (minimum particle number needed for convergence). The PIC code is made parallel using hybrid MPI + OpenMP parallelism, to use as much as possible the shared memory from the available architecture. On Curie, there are 8 cores per socket, which means that the best efficiency can be reached using 1 MPI process per socket and 8 threads per MPI process.

Second test case: 128x128 grid size, 800 million particles, 500 iterations simulation.
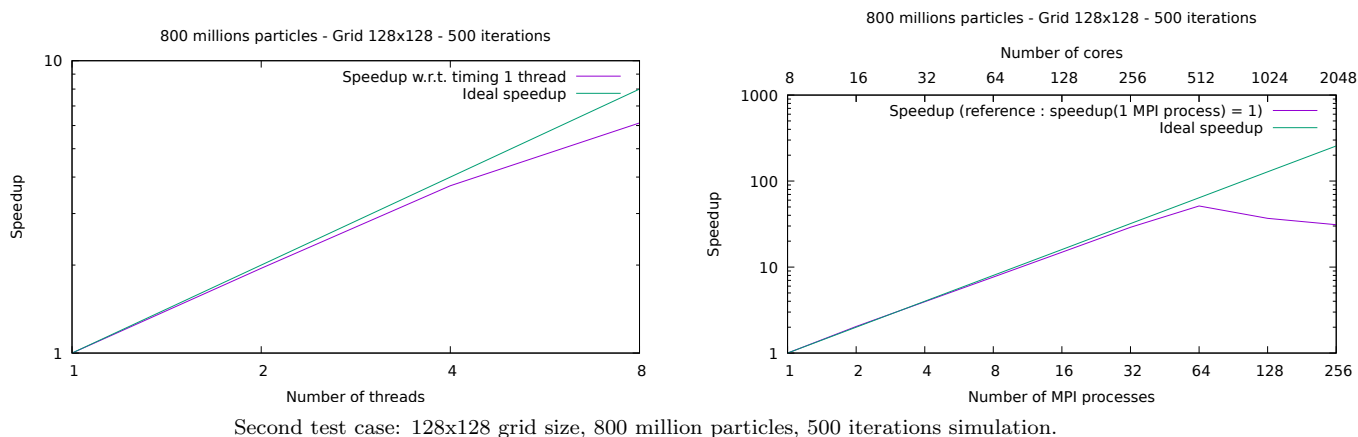
Figure 37: Strong scaling on Curie : OpenMP on one socket (left), Hybrid MPI + OpenMP (right).

The left part shows the performance of the code on 1 socket, using only OpenMP parallelism. The scaling is ideal up to 4 threads and deteriorates on 8 threads. The reason bases on the reduced number of memory channels per socket, 4 precisely, and on the well-known fact that PIC codes are demanding in memory bandwidth. The scalability on 8 threads is thus limited by the number of memory channels. In all, the code processes 39 million particles per second per thread and 238 million particles per second when using 8 threads.

The right part shows that, as long as enough computations are deployed per process, the code has a very good scalability. However, when we reach 128 MPI processes, only 6 million particles are distributed per MPI process. The number of the corresponding computations is clearly not high and therefore the execution time of the simulation is dominated by the communication time between processes.

7 Conclusion

We have performed two-species $2D \times 2D$ simulations with both PIC and semi-Lagrangian methods. Validation of the code is done through dispersion analysis and/or cross comparisons between the results and the numerical parameters. We notice that a high order splitting method in time is relevant, when so many time steps have to be used in this time oscillatory problem that comes from the mass anisotropy. The sixth order splitting scheme

leads to better energy conservation with respect to the classical Strang splitting. The time splitting by direction does however not permit to treat differently the ions and the electrons. So, another splitting scheme by species has been introduced; the latter one permits to use different time steps for the ions and the electrons. In the future, we plan to treat the electrons differently using specific methods (several methods, already proposed in the literature in particular in the PIC case could be tried) in order to speed its computation.

8 Appendix

8.1 Proof of Proposition 3.1

There is a classical lemma that is very useful to prove this proposition

Lemma 8.1. *Let E be a normed vector space and Ω be an open set of $\mathbb{R}^N$. For all $\varepsilon \in [0,1]$, let $f_\varepsilon \in \mathcal{C}^0(\Omega; E)$ be a continuous function such that*

$$\begin{cases} \text{the zeros of } f \text{ are isolated,} \\ f_\varepsilon \text{ locally uniformly converges to } f \text{ on } \Omega \text{ when } \varepsilon \text{ goes to } 0. \end{cases}$$

If there exists a continuous function $x \in C^0(]0,1]; \Omega)$ such that

$$\begin{cases} \forall 0 < \varepsilon \le 1, \ f_\varepsilon(x(\varepsilon)) = 0, \\ x(\varepsilon) \text{ admits a limit point } y \in \Omega \text{ when } \varepsilon \text{ goes to zero,} \end{cases}$$

then y is a zero point of f and x goes to y when ε goes to 0.

Proof. see Appendix 8.2. □

If $\omega_n(\varepsilon)$ do not go to infinity as ε goes to 0, then it admits a limit point. As a consequence, if we apply Lemma 8.1 to $f_\epsilon \equiv D_\epsilon$, $f \equiv \Delta_i \circ \xi_i$, $x \equiv \omega_n$ on the domain $\Omega \equiv \mathbb{C}$, then we deduce that ω_n converges to a zero point of $\Delta_i \circ \xi_i$ as ε goes to 0. We can apply Lemma 8.1, because, on the one hand, since $\Delta_i \circ \xi_i$ is an entire function, its zeros points are isolated, and, on the other hand, D_ε locally uniformly converges to $\Delta_i \circ \xi_i$ as ε goes to 0.

Otherwise, if $\omega_n(\varepsilon)$ goes to infinity and $\varepsilon\omega_n(\varepsilon)$ has a limit point, as ε goes to 0, in the open set

$$\Omega = \{re^{i\theta} \mid r > 0 \text{ and } \theta \in]-\frac{\pi}{4}, \frac{5\pi}{4}[\},$$

then we can apply Lemma 8.1 to $f_\varepsilon \equiv D_\epsilon(\frac{z}{\varepsilon})$, $f(z) \equiv \Delta_e(\frac{z}{\sqrt{2}k})$ and $x(\varepsilon) \equiv \varepsilon\omega_n(\varepsilon)$. Indeed, the hypothesis of uniform convergence on Ω follows of the asymptotic expansion of the plasma dispersion function (13).

Eventually, we can see through the asymptotic expansion of the plasma dispersion function (13) that, if $\omega_n(\varepsilon)$ goes to infinity, $\varepsilon\omega_n(\varepsilon)$ has no limit point in Ω and $-\frac{3\pi}{4}$ or $-\frac{\pi}{4}$ are not limit points of the argument of $\omega_n(\varepsilon)$, then $D_\varepsilon(\omega_n(\varepsilon))$ would go to infinity. But this is impossible because $\omega_n(\varepsilon)$ is a zero point of D_ε. As a consequence, if $\omega_n(\varepsilon)$ goes to infinity and $\varepsilon\omega_n(\varepsilon)$ has no limit point in Ω, then the argument of $\omega_n(\varepsilon)$ converges to $-\frac{3\pi}{4}$ or to $-\frac{\pi}{4}$.

8.2 Proof of Lemma 8.1

Since f_ε goes to f locally uniformly when ε goes to 0, then y is a zero point f. But since the zero points of f are isolated, there exits $\eta_0 > 0$ such that y is the only zero point of f in the ball of center y and of radius η_0.

Now let $0 < \eta < \eta_0$ be a positive number smaller than η_0. By construction and by the compactness of the sphere in $\mathbb{R}^N$, there exists a positive real number $\delta > 0$ such that

$$\forall p \in \Omega, \ |p - y| = \eta \ \Rightarrow \ 0 < \delta \le ||f(p)||_E.$$

But since f_ε goes to f locally uniformly when ε goes to 0, there exists $\varepsilon_0 > 0$ such that

$$\forall 0 < \varepsilon < \varepsilon_0, \forall p \in B(y, \eta_0), \ ||f(p) - f_\varepsilon(p)||_E < \frac{\delta}{2}.$$

As a consequence, if ε is smaller than ε_0 then f_ε has no zero point on the sphere of center y and radius η.

Now by hypothesis, since x is continuous, $x(]0, \varepsilon_0[)$ is a connected set. Furthermore, since y is a limit point of $x(\varepsilon)$ when ε goes to zero, $x(]0, \varepsilon_0[) \cap B(y, \eta) \neq \emptyset$. However, we have shown that $x(]0, \varepsilon_0[) \cap \partial B(y, \eta) = \emptyset$. As a consequence, we deduce that

$$x(]0, \varepsilon_0[) \subset B(y, \eta).$$

Acknowledgment

References

[1] J. W. Banks, R. L. Berger, S. Brunner, B. I. Cohen, and J. A. F. Hittinger. Two-dimensional Vlasov simulation of electron plasma wave trapping, wavefront bowing, self-focusing, and sideloss. *Physics of Plasmas*, 18(5):052102, 2011.

[2] R. L. Berger, S. Brunner, J. W. Banks, B. I. Cohen, and B. J. Winjum. Multi-dimensional Vlasov simulations and modeling of trapped-electron-driven filamentation of electron plasma waves. *Physics of Plasmas*, 22(5):055703, 2015.

[3] N. Besse, J. Segré, and E. Sonnendrücker. Semi-Lagrangian schemes for the two-dimensional Vlasov-Poisson system on unstructured meshes. *Transport Theory and Statistical Physics*, 34(3-5):311–332, 2005.

[4] C. K. Birdsall and A. B. Langdon. Plasma physics via computer simulation. 2004.

[5] S. Blanes and P. C. Moan. Practical symplectic partitioned Runge–Kutta and Runge–Kutta–Nyström methods. *Journal of Computational and Applied Mathematics*, 142(2):313–330, 2002.

[6] J. D. Callen. Special functions. In *Fundamentals of Plasma Physics*, chapter Appendix B. Madison, Wisconsin, draft edition, june 2006.

[7] F. Casas, N. Crouseilles, E. Faou, and M. Mehrenberger. High-order Hamiltonian splitting for the Vlasov–Poisson equations. *Numerische Mathematik*, pages 1–33, 2016.

[8] E. Chacon-Golcher, S. A. Hirstoaga, and M. Lutz. Optimization of Particle-In-Cell simulations for Vlasov-Poisson system with strong magnetic field. *ESAIM: Proc.*, 53:177–190, 2016.

[9] C.Z. Cheng and G. Knorr. The integration of the Vlasov equation in configuration space. *J. Comput. Phys.*, 22:330–351, 1976.

[10] N. Crouseilles, M. Gutnic, G. Latu, and E. Sonnendrücker. Comparison of two Eulerian solvers for the four-dimensional Vlasov equation: Part II. *Communications in Nonlinear Science and Numerical Simulation*, 13(01):94–99, 2008.

[11] J. Denavit. First and Second Order Landau Damping in Maxwellian Plasmas. *Physics of Fluids*, 8(3):471–478, 1965.

[12] F. Filbet and E. Sonnendrücker. Comparison of Eulerian Vlasov solvers. *Computer Physics Communications*, 150(3):247 – 266, 2003.

[13] F. Filbet and E. Sonnendrücker. Modeling and numerical simulation of space charge dominated beams in the paraxial approximation. *Mathematical Models and Methods in Applied Sciences*, 16(05):763–791, 2006.

[14] F. Filbet, E. Sonnendrücker, and P. Bertrand. Conservative numerical schemes for the Vlasov equation. *Journal of Computational Physics*, 172(1):166 – 187, 2001.

[15] K. Kormann. A semi-Lagrangian Vlasov solver in tensor train format. *SIAM Journal on Scientific Computing*, 37(4):B613–B632, 2015.

[16] L. Landau. On the vibrations of the electronic plasma. *J. Phys. USSR*, 10:25–34, 1946. (Also in Russian: "O kolebaniiakh elektronnoi plazmy", Zhurnal Eksperimental'noi i Teoreticheskoi Fiziki 16, 574 (1946)).

[17] M. Lesur. Method and scheme-independent entropy production in turbulent kinetic simulations. *Computer Physics Communications*, 200:182 – 189, 2016.

[18] M. Badsi and M. Herda. Modelling and simulating a multispecies plasma. *ESAIM: Proc.*, 53:22–37, 2016.

[19] E. Madaule, M. Restelli, and E. Sonnendrücker. Energy conserving discontinuous Galerkin spectral element method for the Vlasov-Poisson system. *Journal of Computational Physics*, 279:261 – 288, 2014.

[20] M. Mehrenberger, C. Steiner, L. Marradi, N. Crouseilles, E. Sonnendrücker, and B. Afeyan. Vlasov on GPU (VOG project). *ESAIM: Proc.*, 43:37–58, 2013.

[21] T. Nakamura and T. Yabe. Cubic interpolated propagation scheme for solving the hyper-dimensional Vlasov-Poisson equation in phase space. *Computer Physics Communications*, 120(2):122 – 154, 1999.

[22] M. Shalaby, A. E. Broderick, P. Chang, C. Pfrommer, A. Lamberts, and E. Puchwein. SHARP: A spatially higher-order, relativistic Particle-in-Cell code. *The Astrophysical Journal*, 841(1):52, 2017.

[23] M. M. Shoucri and R. R. T. Gagné. A multistep technique for the numerical solution of a two-dimensional Vlasov equation. *Journal of Computational Physics*, 23(3):242 – 262, 1977.

[24] D. A. Silantyev, P. M. Lushnikov, and H. A. Rose. Langmuir wave filamentation in the kinetic regime. ii. Weak and strong pumping of nonlinear electron plasma waves as the route to filamentation. *Physics of Plasmas*, 24(4):042105, 2017.

[25] E. Sonnendrücker. Numerical Methods for the Vlasov-Maxwell equations. book in preparation, version of february 2015.

[26] T. Umeda, S. Ueno, and T. K. M. Nakamura. Ion kinetic effects on nonlinear processes of the Kelvin-Helmholtz instability. *Plasma Physics and Controlled Fusion*, 56(7):075006, 2014.